Available online at www.sciencedirect.com

ScienceDirect

Geochimica et Cosmochimica Acta 243 (2018) 186–204

Geochimica et Cosmochimica Acta

www.elsevier.com/locate/gca

Genesis of mud volcano fluids in the Gulf of Cadiz using a novel basin-scale model approach

Christopher Schmidt [a,*], Ewa Burwicz [a], Christian Hensen [a], Klaus Wallmann [a], Sara Martínez-Loriente [b], Eulàlia Gràcia [c]

[a] GEOMAR Helmholtz Centre for Ocean Research Kiel, Wischhofstr. 1-3, 24148 Kiel, Germany
[b] iCRAG (Irish Centre for Research in Applied Geosciences), UCD School of Earth Sciences, Belfield, Dublin 4, Ireland
[c] B-CSI, Institut de Ciències del Mar, CSIC, Pg. Marítim de la Barceloneta, 37-49, 08003 Barcelona, Spain

Received 18 October 2017; accepted in revised form 14 September 2018; Available online 28 September 2018

Abstract

Mud Volcanism and fluid seepage are widespread phenomena in the Gulf of Cadiz (SW Iberian Margin). In this seismically active region located at the boundary between the African and Eurasian plates, fluid flow is typically focused on deeply rooted active strike-slip faults. The geochemical signature of emanating fluids from various mud volcanoes (MVs) has been interpreted as being largely affected by clay mineral dehydration and recrystallization of Upper Jurassic carbonates. Here we present the results of a novel, fully-coupled 1D basin-scale reactive-transport model capable of simulating major fluid forming processes and related geochemical signatures by considering the growth of the sediment column over time, compaction of sediments, diffusion and advection of fluids, as well as convective and conductive heat flow. The outcome of the model is a realistic approximation to the development of the sediment pore water system over geological time scales in the Gulf of Cadiz. Combined with a geochemical reaction transport model for clay mineral dehydration and calcium carbonate recrystallization, we were able to reproduce measured concentrations of Cl, strontium and $^{87}Sr/^{86}Sr$ of emanating mud volcano fluids. These results support previously made qualitative interpretations and add further constraints on fluid forming processes, reaction rates and source depths. The geochemical signature at Porto MV posed a specific problem, because of insufficient constraints on non-radiogenic $^{87}Sr/^{86}Sr$ sources at this location. We favour a scenario of basement-derived fluid injection into basal Upper Jurassic carbonate deposits (Hensen et al., 2015). Although the mechanism behind such basement-derived flow, e.g. along permeable faults, remains speculative at this stage, it provides an additional source of low $^{87}Sr/^{86}Sr$ fluids and offers an idea on how formation water from the deepest sedimentary strata above the basement can be mobilized and eventually initiate the advection of fluids feeding MVs at the seafloor.

The dynamic reactive-transport model presented in this study provides a new tool addressing the combined simulation of complex physical-geochemical processes in sedimentary systems. The model can easily be extended and applied to similar geological settings, and thus help us to provide a fundamental understanding of fluid dynamics and element recycling in sedimentary basins.

Keywords: Gulf of Cadiz; Mud Volcanism; Reactive Transport Modeling; Clay dehydration; Carbonate recrystallization; Fluid flow

1. INTRODUCTION

Fluid seepage and mud volcanoes (MVs) have been ubiquitously observed on- and offshore on earth. Several thousand MVs worldwide have been described in diverse

* Corresponding author.
E-mail address: cschmidt@geomar.de (C. Schmidt).

https://doi.org/10.1016/j.gca.2018.09.011
0016-7037/

tectonic environments. To date, the majority of these features are located in compressional tectonics settings (e.g. Milkov, 2000; Kopf, 2002; Mazzini and Etiope, 2017). Cold seeps and MVs play an important role for the global element budget of hydrocarbons, such as CO_2 and CH_4 and some other major elements such as Sr, B or Li (Kopf, 2003; Milkov et al., 2003). The emanated fluid composition of MVs typically differs from seawater (Kopf, 2002). However, deviations from seawater are not uniform and vary according to underlying processes, such as the transformation of clay minerals (Kastner et al., 1991; Hensen et al., 2004), microbial mineralization of organic matter (Martin et al., 1993; Fehn et al., 2007; Tomaru et al., 2007), high temperature interactions with sediment and rocks (Martin et al., 1991; Mazzini et al., 2017), dissolution and recrystallization of carbonates (Martin et al., 1996; Luff and Wallmann, 2003; Castellini et al., 2006), formation and dissociation of gas hydrates (Kopf, 2002; Hensen et al., 2004, 2007; Paull et al., 2015), and rise of salt-diapirs and dissolution of evaporites (Charlou et al., 2003; Reitz et al., 2007; Haffert et al., 2013).

During the last two decades numerous multidisciplinary studies have been carried out to better understand mud volcanism and underlying processes in the Gulf of Cadiz (GoC; Fig. 1; Gràcia et al., 2003a,b, 2010; Pinheiro et al., 2003; Somoza et al., 2003; Hensen et al., 2007, 2015; Medialdea et al., 2009; Nuzzo et al., 2009; Scholz et al., 2009, 2010a,b; Bartolome et al., 2012; Haffert et al., 2013; Martínez-Loriente et al., 2013, 2018; Toyos et al., 2016). Here, most of the known MVs are found along lineaments crossing the accretionary wedge, e.g. Captain Arutyunov MV (CAMV) or Porto MV (Fig. 1). Only a few MVs, including Abzu MV, Tiamat MV, and M. Ivanov MV (also referred as ATI MVs), were discovered along a major strike-slip fault system outside the accretionary wedge (Fig. 1), and hence outside their typical tectonic setting (Hensen et al., 2015).

In general, most of the MVs on the accretionary wedge show a strong dilution of conservative elements, e.g. Cl compared to modern seawater (Hensen et al., 2007; 2015; Scholz et al., 2009; Haffert et al., 2013). In combination with a characteristic $\delta^{18}O/\delta D$ signature, the pore water freshening is a clear indicator for clay mineral dehydration (i.e. smectite to illite transformation; Hensen et al., 2015). Clay mineral dehydration is most pronounced on the upper continental margin and decreasing westward (Scholz et al.,

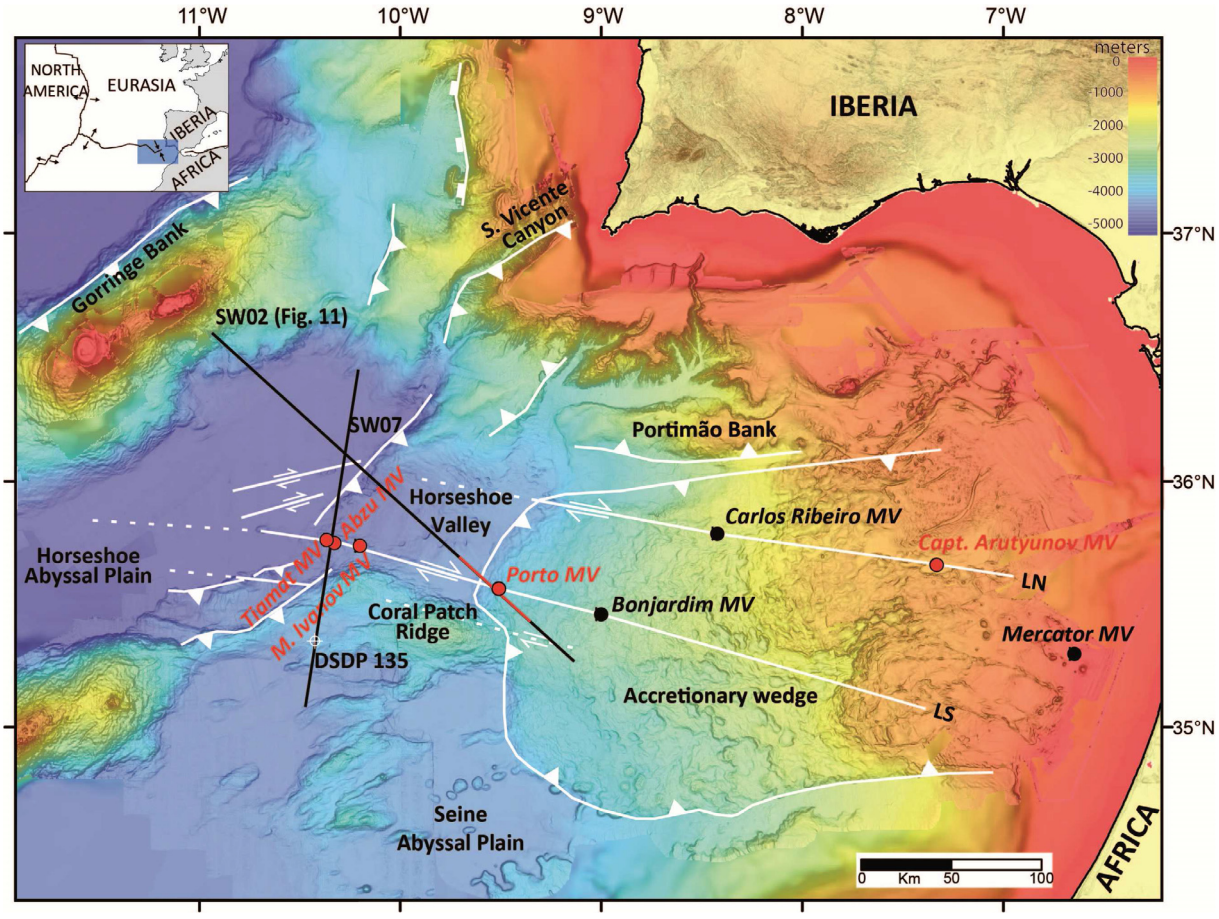

Fig. 1. Bathymetric map (modified after Hensen et al., 2015) of the Gulf of Cadiz and the surrounding areas in the NE Atlantic Ocean from a ~90 m digital grid (Zitellini et al., 2009). White lines depict the main tectonic features in the region LS: lineament south; LN: lineament north (Bartolome et al., 2012). Black circles represent some selective MVs, while red circles label the 5 representative MVs used in this study. Black lines represent the seismic line SW02 (Martínez-Loriente et al., 2018) across the Horseshoe abyssal plain and over Porto MV, and seismic line SW07 (Hensen et al., 2015) across ATI MVs and DSDP site 135.

2010b). Some MVs on the upper slope show highly enriched Cl concentrations due to the dissolution of evaporites (e.g. CAMV and Mercator MV in Fig. 1; Hensen et al., 2007; Haffert et al., 2013). MVs in the west of the GoC, such as ATI MVs and Porto MV show higher δD and lower $\delta^{18}O$ values accompanied by a strong enrichment of Sr with a low Sr isotope ratio. These findings have been interpreted as recrystallization of carbonates (Hensen et al., 2015).

To explain the fluid composition observed at Porto MV the advection of crustal derived fluids with $^{87}Sr/^{86}Sr$ ratios of 0.704 or below has been hypothesized (Scholz et al., 2009; Hensen et al., 2015). Fluid advection trough oceanic crust of an age older than 140 Ma is a process that has not been verified by geochemical evidence of active seepage up to date. Results of previous studies (e.g. Stein et al., 1995) propose that fluid advection in oceanic crust older than ≈65 Ma is usually inhibited by thick layers of impermeable sediments accumulating over an old oceanic crust. However, Von Herzen (2004) showed that fluid advection along strong topographic contrasts in the crust is possible in oceanic crust older than 65 Ma. Furthermore, seismic studies at the Tydeman fracture zone in the tropical Atlantic Ocean (e.g. Calvert and Potts, 1985) indicate that fluid flow through several faults affecting oceanic crust older than 80 Ma maybe still active, and Fisher and Von Herzen (2005) show evidence for fluid advection in 106 Ma old oceanic crust of the Madeira Abyssal Plain.

The approach of the current manuscript is to use numerical methods to improve a general, quantitative understanding of fluid formation processes in sedimentary basins related to geochemical processes and the potential role of fluid advection through old oceanic crust. Mud volcano fluids typically provide a window into the processes occurring underneath. To date, however, interpretations were mostly based on conventional methods only, such as property-property plots of fluid data or simple numerical models used to draw conclusions about fluid sources or fluid advection rates in surface sediments. To overcome this lack of knowledge, we designed a novel, basin-scale reactive transport model to simulate and quantify important fluid forming processes, such as the ubiquitous smectite to illite transformation, constrained by geochemical tracers in the pore fluid. The procedure described below enables the determination of the quantitative interaction of major processes affecting pore fluid geochemistry, and provides a more reliable approximation to the formation at depth of mud volcano fluids and their implications for processes that induce upward advection.

2. GEOLOGICAL SETTING OF THE GULF OF CADIZ

The GoC, located SW of the Iberian Peninsula in the NE Atlantic Ocean, has undergone a complex tectonic history (Maldonado et al., 1999). The opening of the Central Atlantic Ocean in the Early Jurassic (e.g. Rovere et al., 2004), represented the development from a passive continental margin into a convergent margin (Gràcia et al., 2003b; Duarte et al., 2013). The WNW – ESE running South West Iberian Margin (SWIM) fault system, a diffusive deep rooted strike-slip fault system (Bartolome et al., 2012), marks the boundary between the African and Eurasian plates (Zitellini et al., 2009). The convergence between the African and Eurasian plates in the GoC started in the Oligocene and continues with a present-day convergence of 4–5 mm a^{-1} (Argus et al., 1989; Schettino and Turco, 2009). In the late Tortonian, the progression of the Gibraltar Arc into the Atlantic Ocean, and the coeval subduction and detachment of the oceanic plate in the Alboran Sea (Wortel and Spakman, 2000), caused the development of a U-shaped accretionary wedge in the GoC (Duarte et al., 2013). Numerous authors suggested that the progression of the arc into the Atlantic Ocean ceased at the beginning of the Pliocene (e.g. Lonergan and White, 1997). However, Gutscher et al. (2012) suggested that subduction remained active until today. The main tectonic structures identified in the GoC are NE-SW trending thrust faults (Gràcia et al., 2003b; Zitellini et al., 2004; Martínez-Loriente et al., 2013, 2018), and WNW-ESE trending strike-slip faults (Terrinha et al., 2009; Zitellini et al., 2009; Bartolome et al., 2012; Martínez-Loriente et al., 2013, 2018). The GoC is a seismically active region where two large earthquakes occurred in the last 300 years. For instance, the 1755 the great Lisbon earthquake with an estimated magnitude of $M_w > 8.5$, which combined with a destructive tsunami devastated the city of Lisbon (Baptista et al., 1988). The most recent great earthquake occurred in 1969, in the Horseshoe Abyssal Plain with a magnitude of about $M_w = 7.9–8.0$ (Fukao, 1973). A total of eight events of great magnitude ($Mw \sim 8$) occurred in the area during the Holocene (Gràcia et al., 2010).

The seismo-stratigraphic interpretation of the GoC and the Horseshoe abyssal plain is based on the results of the DSDP Site 135 on the Coral Patch Ridge (Fig. 1; Hayes et al., 1972). By using multichannel seismic profiles of the SWIM dataset, Martínez-Loriente et al. (2013) defined the seismo-stratigraphy of six main units. The uppermost unit I is composed of Upper Oligocene to Quaternary age sediments. Unit II is characterized by terrigenous sediments from Upper Cretaceous to Lower Eocene age. Units III–IV are built-up of terrigenous sediments from Cretaceous and Lower Cretaceous. Unit V, contain Upper Jurassic carbonates, which are underlain by the basement (Unit VI). The basement is composed of different domains, however, below the area of ATI MVs, the oceanic crust is of Early Jurassic age (Martínez-Loriente et al., 2014). All units highly vary in their thickness. On the basis of geochemical findings, the 10 km thick accretionary wedge (Gutscher et al., 2009) on the easternmost part of the GoC is built mainly of terrigenous material, with no evidence of Upper Jurassic carbonates underneath (Hensen et al., 2015).

3. REACTIVE-TRANSPORT MODEL

3.1. General concept

In this study, we present a newly developed vertical 1D fully-coupled basin-scale reaction-transport model. We approximately reconstruct the sedimentary sequences with their physical properties over time. The reaction-transport part accounts for clay mineral dehydration and carbonate

recrystallization, as well as the advection of fluids through aged oceanic crust. Overall, five dissolved (Ca, Cl, K, Na, Sr, and ^{87}Sr) and four solid (smectite, illite, carbonate, strontium) species are considered in the model. We used MATLAB R2014a (The MathWorks Inc.) to implement the non-steady-state model. An advantage of this model is the adaptive numerical mesh, which simulates the growing sediment column over time with a progressive compaction of the sediments. With this method, we are able to simulate the spatial and temporal evolution of the sedimentary sequences of the GoC. The governing transport equations as well as temperature and pressure equations of the model approach can be found in the appendix.

3.2. Reaction solver

3.2.1. Clay dehydration

A widespread dehydration reaction causing substantial pore fluid freshening in marine sediments is the transformation of smectite to illite (Brown et al., 2001). Freshening is caused by the release of interlayer H_2O, which typically ranges from 20 to 25 wt% of the minerals (Fitts and Brown, 1999). Numerous studies, mostly based on deep ODP/IODP drilling data and MV fluids, have shown that this dehydration process causes dilution of conservative elements, e.g. Cl and the release of fluid mobile elements like Li, B and Sr (Chan and Kastner, 2000; Scholz et al., 2009, 2010a). The usual temperature range for this process appears to be between 60 °C and 150 °C (Kastner et al., 1991; Hensen et al., 2004). For this reaction, various numerical models have been described in the literature. In this study, we use a modified model by Cuadros and Linares (1996) where the reaction rate is defined as:

$$R_{Clay} = S^{\alpha} * (K^{+})^{\beta} * k \quad (1)$$

where S – *smectite/(smectite + illite)*, K^+ – dissolved concentration of K, α and β – rate order parameters for smectite and K, and k – depth dependent rate constant. In contrast to Cuadros (2006), we used an Arrhenius type, temperature dependent reaction rate which reads as follows:

$$k = A * exp\left(\frac{-E}{R*(T+273.15)}\right) \quad (2)$$

where A – frequency factor, E – activation energy, and R – universal gas constant.

The amount of Sr released into the pore fluid is determined after following equation:

$$R_{Sr} = \frac{R_{Clay}}{100} * \rho_s * \left(\frac{1-\theta}{\theta}\right) * 10^6 * M_{Smectite} * X_{Sr} \quad (3)$$

where R_{clay} is the reaction rate of Eq. (1) in (wt%), the factor of 10^6 is introduced to achieve the unit of μM, $M_{Smectite}$ is the molar weight of smectite and X_{Sr} is the portion described as a ratio of Sr in smectite.

3.2.2. Carbonate recrystallization

At seafloor pressure and temperature conditions marine carbonate deposits typically undergo a process called recrystallization. This process includes micro-solution and precipitation of carbonates to transfer the carbonate phase into a thermodynamic more stable state (Morse and Mackenzie, 1990). This process has been inferred from observations made on DSDP/ODP drill cores; most notably, the increase of Sr in ambient pore water after deposition (Richter and DePaolo, 1987; Fantle and DePaolo, 2006; Fantle, 2015). Obviously, biogenic carbonates undergo a transformation into a more stable form of calcite. While the composition and texture are largely maintained (Baker et al., 1982), grain growth is concomitant (Morse and Casey, 1988).

For our numerical model approach we adapted a kinetic rate for Sr release due to the recrystallization of bulk carbonate as suggested by Richter and DePaolo (1987):

$$\frac{\delta C_{Sr}}{\delta t} = \left(ds * \frac{(1-\theta)}{\theta}\right) * R_{age} * \left(C_S - K * C_f\right) \quad (4)$$

where C_{Sr} – concentration of *Sr* released into the pore fluid, C_s and C_f – concentrations of Sr in solid and in fluid respectively, R_{age} – rate parameter, and K – effective distribution coefficient. For numerical reasons we could not use the carbonate concentrations directly. Therefore, we implemented an additional solid species called Sr concentration of carbonates in the model.

The rate parameter for the recrystallization reads as follows

$$R_{age} = R_{\alpha} + R_{\beta} * exp^{\left(\frac{-age}{R_{\gamma}}\right)} \quad (5)$$

in 1/Ma where R_α, R_β and R_γ are model constants, and *age* is the sediment age. R_α is the parameter that controls the long-term recrystallization where R_β and R_γ control the early recrystallization.

3.2.3. Fluid injection from basement

The injection from the basement into the basal sediment column for the Porto case study in scenario 4 is solved by using the pressure solver of the numerical model. When activated, at each time step an additional water mass, in kg s^{-1} m^{-2}, was injected with a distinct chemical composition to the lowermost model knot. In the following time step, this pressure pulse starts to be equilibrated resulting in an additional advective component in the model column.

3.2.4. Strontium isotopes

The strontium isotopic ratio of $^{87}Sr/^{86}Sr$ is calculated after Hoefs (2004)

$$\Phi_{87} = \frac{^{87}Sr}{^{84}Sr + {}^{85}Sr + {}^{86}Sr + {}^{87}Sr} = \frac{^{87}Sr}{Sr} = \frac{R_{87}}{9.43 + R_{87}} \quad (6)$$

with Φ_{87} – mol fraction of ^{87}Sr, R_{87} – ratio of $^{87}Sr/^{86}Sr$, and the constant 9.43 is defined by the abundance of other Sr isotopes. Due to the fact that the ratio of $^{87}Sr/^{86}Sr$ cannot be transported as a species, the bulk concentration of Sr, as well as ^{87}Sr are handled separately in the model domain. From the geological record of $^{87}Sr/^{86}Sr$ in marine carbonates (McArthur et al., 2001), the concentration of ^{87}Sr can be defined through earth history using Eq. (6). The two Sr species, Sr and ^{87}Sr, can react and are transported

in the sediment column. At the end of the simulation values of ^{87}Sr and Sr are used to calculate $^{87}Sr/^{86}Sr$ as model output.

3.3. Boundary conditions and initial conditions

3.3.1. Dissolved species

Several upper and lower boundary conditions were applied in the case studies; Table 1 shows a compilation of all boundary conditions. The upper boundary conditions (UBC) for the dissolved species Cl, Na and K are set to a constant modern seawater-like concentration (Cl = 557 mM; Na = 477 mM; Demicco et al., 2005) and concentration of 10 mM for K (Horita et al., 2002). For Ca, variations through Earth's history in seawater over the past are published by Horita et al. (2002). For Sr, the Sr/Ca ratio from Steuber and Veizer (2002) and the Ca concentration was taken to determine the Sr concentration in seawater over time. The $^{87}Sr/^{86}Sr$ ratio of seawater over time is available from McArthur et al. (2001) and has been used to determine the concentration of ^{87}Sr. The variations trough time for Ca, Sr/Ca, Sr and $^{87}Sr/^{86}Sr$ are shown in Fig. 2. For all scenarios, the UBC is an open boundary.

For the first two case studies and Porto MV case study scenario 1 to 3, closed boundary conditions are applied to the lower boundary, effectively resulting in a zero-gradient boundary condition for diffusive transport and in a no flow boundary condition for advection. In the fourth scenario of Porto MV case study, the lower boundary is treated as an open boundary for diffusion and for advection to allow for fluid inflow through the base of the sediment column. Here, fixed concentrations are applied to the injected fluids. In this scenario, we tested the potential effect of the injection of crustal derived fluids on the pore water composition, predominantly with respect to variations in Sr, $^{87}Sr/^{86}Sr$, and Cl. Fluids circulating in the oceanic crust (lower boundary) are difficult to constrain, essentially, because data from this or a similar, deeply buried site are generally unavailable. Useful constraints are only available from hydrothermal vents, ridge flank systems or old, less deeply buried crust sections. Hydrothermal vent solutions typically have $^{87}Sr/^{86}Sr$ values between 0.7030 and 0.7040, Sr concentrations close to or slightly enriched with respect to normal seawater and variable Cl concentrations depending on the occurrence of subsurface phase separation (e.g. Douville et al., 2002). Known ranges of values from ridge-flank systems (up to ~60 °C) are between 0.70715 and 0.70745 for $^{87}Sr/^{86}Sr$, Sr concentrations up to 130 µM and normal chlorinity (e.g. Wheat et al., 2000). On the basis of the available measurements and that fact the crustal

Table 1
Boundary conditions of all case studies and modeled scenarios.

	UBC	LBC	Diffusion LBC	Advection LBC
Case study 1 + 2Case study 3 (scenario 1–3)	Open	Closed	Zero gradient diffusion	No flow
Case study 3 (scenario 4)	Open	Open	Concentration gradient	Inflow

(1) UBC: Upper boundary condition; (2) LBC: Lower boundary condition.

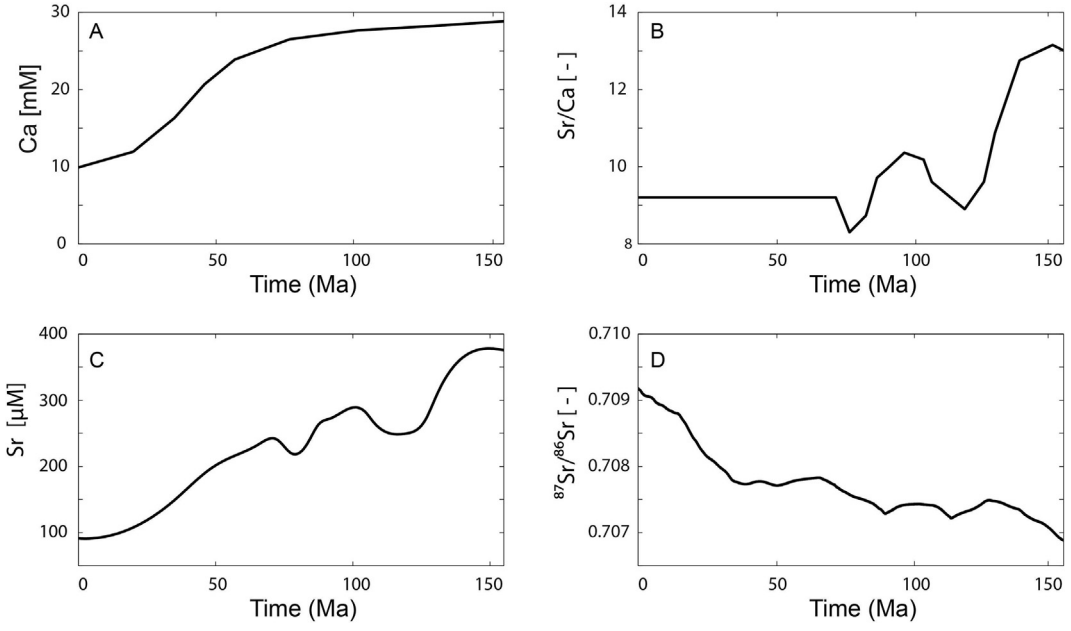

Fig. 2. Upper boundary conditions for the last 155 Ma; A: Ca; B; Sr/Ca; C: Sr; D: $^{87}Sr/^{86}Sr$.

temperatures are ~150 °C below Porto MV, we use a hypothetical fluid composition with $^{87}Sr/^{86}Sr$ of 0.706, Sr concentrations of 130 μM and normal seawater chlorinity. In addition to that, several test runs have shown that the impact of a change of ±25 μM in Sr and ±0.002 in the isotope ratio has just a small impact in the overall result.

3.3.2. Solid species

The sediment input over the whole model period of ~155 Ma was generally characterized by the deposition of smectite, illite, and calcium carbonate. The aim was not to build a detailed reconstruction of the sedimentary history, but rather to analyse the geochemical impact caused by the change from carbonate-dominated sedimentation to terrigenous sedimentation in the early Cretaceous.

Initial conditions for the solid phase were set for smectite to 70 wt% and illite 15 wt%. Since no information on the clay mineral composition at DSDP Site 135 was available, we used data from the DSDP Site 398 at the Vigo Seamount off Northwest Iberia with similar sedimentary units compared to DSDP Site 135 in order to constrain our assumptions. At DSDP Site 398, smectite contents average between 40 and 60% (Chamley et al., 1979). Further evidence for the deposition of smectite-rich sediments comes from DSDP Site 547 on the Morocco continental margin, where clay mineral content is up to 90% with a smectite fraction of more than 70 wt% (Chamley and Debrabant, 1984). However, measured smectite contents represent values mostly after smectite to illite transformation occurred so that a higher input (above measured average concentrations) seems to be a reasonable assumption. Sr isotope ratios for clay minerals were defined using the values measured in mud clasts, sampled from the MVs, varying between 0.7095 and 0.7120 (Hensen et al., 2015). Therefore, we used an average isotope ratio of 0.710 in the model.

As for the clay mineral composition, also no bulk data for Jurassic carbonate deposits are available for the Gulf of Cadiz. DSDP Site 135 did not reach the depth of Jurassic deposits. However, the Western Atlantic counterpart to DSDP Site 135, DSDP Site 105 reached Upper Jurassic layers described as clayey limestones (Hollister et al., 1972), suggesting a carbonate content of about 70 wt%. If Upper Jurassic carbonates are present in the sediment column of the model, we assume 70 wt% of calcium carbonate. Carbonate deposits contain isotopic ratio of the time of their deposition. For Upper Jurassic Carbonates a isotopic ratio of 0.7068 corresponds to the seawater ratio at 155 Ma (Fig. 2D; McArthur et al., 2001).

Eq. (4) requires the Sr concentration of carbonates. To solve this numerically stable a fourth solid species was introduced. To determine the initial condition, we used the following equation to approximate the Sr concentration of carbonates:

$$C_s = \frac{C_{Carbonate}}{100} * \rho_s * \frac{0.4}{M_{Ca}} * D_{Sr} * \frac{Sr^{2+}}{Ca^{2+}} \quad (7)$$

where C_s is the concentration of Sr in carbonate (in μM), $C_{arbonate}$ is the carbonate concentration (in wt%), the factor of 0.4 is introduced since only 40 wt% of $CaCO_3$ is Ca, M_{Ca} is the molar weight of Calcium, D_{Sr} is the Sr distribution coefficient between seawater and carbonate, Sr^{2+}/Ca^{2+} is the seawater ratio of Sr and Ca. The distribution coefficient for deep sea carbonates after Stoll et al. (1999) is $D_{Sr} = 0.176$.

3.4. Solution algorithm

At the beginning of each model run, initial states of lithostatic pressure, pore fluid pressure, effective stress, porosity and temperature are initialized. The two first grid nodes with a cell size of 5 meter are predetermined. Each time step starts with the deposition of a new sediment layer. Therefore, the lithostatic pressure and the pore pressure solutions are updated by using the Finite Element (FE) scheme. Based on the new lithostatic and pore pressure calculations, a new effective stress is obtained for each of the grid nodes. The change in the effective stress field determines the degree of porosity reduction (i.e. compaction), which is performed on every mesh node.

Finally, the reference frame adjustment takes place and results in the growing of the sediment column and the new top node marking the seafloor. Based on the new pressure, the density of fluids, permeability, and the Darcy velocity for the fluid is recalculated. Darcy velocity is used to determine the state of the boundary condition at every time step. Upper boundary conditions adapt automatically according to the presence of the potential venting induced by the additional pore fluids entering the system (i.e. pore fluid refreshening due to the smectite-illite transition). The temperature equation is solved for diffusion (FE) and advection (Finite Volume – FV) for the solid and fluid phase. The diffusion coefficients are determined using the new temperature profile. Advection and diffusion of each solute are solved separately using a FV and a FE scheme, respectively.

The last part of the solution algorithm contains the geochemical reactions. To maintain the numerical stability of the code, a sub-stepping method is applied to the geochemical reaction solver. This method adjusts the main model time-step to the rates of kinetically-resolved chemical reactions, which are commonly much faster than the transport steps. The sub-steps are solved within the main model loop. First, the smectite-illite transformation with the release of freshwater and Sr is accomplished, followed by the recrystallization of carbonates, and the release of Sr into the ambient pore waters. At the end of each time step, the isotope ratio for Sr is computed.

4. MODEL CASE STUDIES

The numerical model approach is tested in three case studies, which show a characteristic fluid composition for their location within the GoC. In a first case study based on CAMV, we tested the ability of the model to simulate clay dehydration, which apart from evaporite dissolution (not considered in this study), is the dominant fluid forming process on the upper continental slope. The ATI MVs were used as a case study to test the interplay of carbonate recrystallization and clay dehydration as source for the mud volcano fluids. For Porto MV, we tested the combination of both mineral reaction and the advective inflow of

fluids trough altered oceanic crust. Parameters used for different model scenarios of the reaction package can be found in the appendix.

4.1. Case study I: Captain Arutyunov MV

CAMV is located on the upper continental margin at 850 m water depth. Using Cl concentrations corrected for evaporite dissolution after Hensen et al. (2007), this MV shows very low Cl concentrations of ≈160 mM. At the same time, Sr concentrations are well above 790 μM with a pronounced radiogenic isotopic ratio of 0.7099 on average. The underlying sediments of the MV are of terrigenous origin within the accretionary wedge. The sediment column has a thickness of up to 9 km (Gutscher et al., 2009), and the oldest sediments above the crust are presumably of Late Cretaceous age (Hensen et al., 2015). Based on the age of the sediments, the model run time is set to 135 Ma. The key reaction is clay dehydration, where the activation energy and the frequency factor of the Arrhenius type reaction rate equation (Eq. (2)), as well as the temperature are the most crucial parameters. Values for the activation energy and the frequency factor, which can be found in the literature, are distributed over a brought range. After Cuadros and Linares (1996) the activation energy needed for the transformation of smectite to illite can be between 13,000 and 140,000 J mol^{-1}. The frequency factor varies over several orders of magnitude (Pytte and Reynolds, 1989; Huang et al., 1993). Below, we show three model runs for CAMV to calibrate the reaction to the measured data. The three scenarios consider: (1) low activation energy combined with a low frequency factor, (2) high activation energy combined with a high frequency factor, and (3) medium activation energy combined with a low frequency factor.

In the first scenario, the transformation from smectite to illite starts almost on the seafloor, at a temperature of 4 °C (Fig. 3). According to the present-day thermal limits of the reaction of 50–160 °C (shaded area in Fig. 3), this scenario is unrealistic. With a high activation energy tested in the second scenario, we see the opposite effect on the reaction. The smectite to illite transformation starts at a temperature of more than 80 °C. Medium activation energy like in scenario 3, results in a smectite to illite transformation which begins at about 50 °C in 1.5 km sediment depth. The highest decrease of smectite and increase of illite can be seen between 4 and 6 km depth. Downwards, the reaction slows down again due to the smaller smectite amount in the sediment.

Nevertheless, all three scenarios result in low Cl concentrations with less than 200 mM (Fig. 4A), but the profiles show a different behavior for the various scenarios. The Sr concentration released by the reaction is controlled by the reaction rate (see Eq. (3); Fig. 4B). The isotopic ratio of $^{87}Sr/^{86}Sr$ released from clays is set to 0.7100 in all scenarios (according to data reported by Hensen et al., 2015). This value is reached from a depth of 4 km downwards (Fig. 4C). The profiles reveal considerable differences that are explained by the differing onset of clay-mineral dehydration and diffusive exchange with seawater. Comparing the modeling results to measured concentrations of CAMV, it is clear that the model approach is able to reproduce the observed fluid signature for all three scenarios, in a sediment depth between 5.5 km and 7.5 km (Fig. 4). In summary, the third scenario delivers the most satisfying results. In comparison to previous studies where this numerical model of clay dehydration has been applied (e.g. Cuadros, 2006), the observed decrease of smectite in this scenario is the most realistic one.

The third critical parameter for clay dehydration is the temperature. The model considers convection and conduction of heat to determine the temperature distribution using a heat flow at the lower boundary of the model domain, and the constant T_0 value at the seafloor surface. Measurements of modern heat flow data by Grevemeyer et al. (2009) show a value of ∼45 mW m^{-2} in the east and ∼60 mW m^{-2}

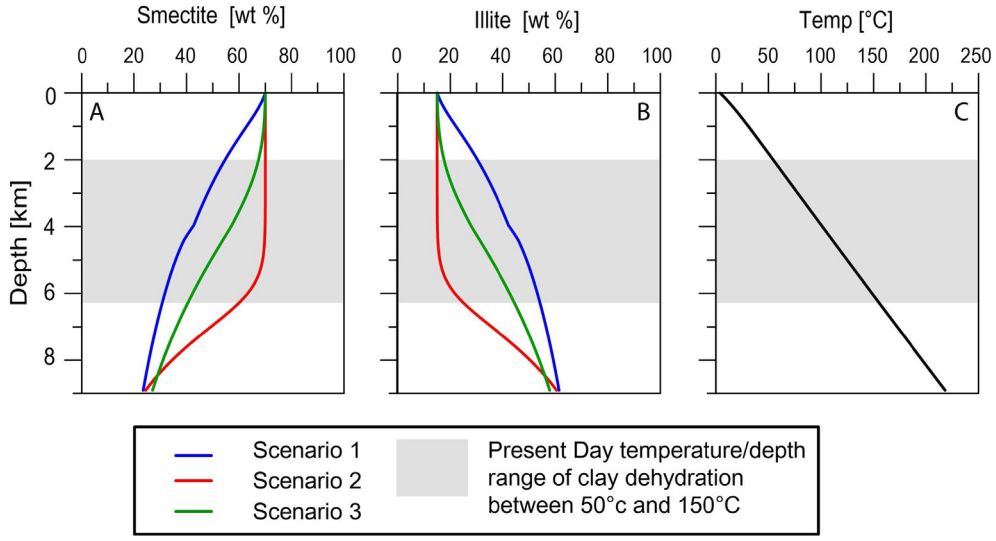

Fig. 3. Depth profile for solids of CAMV (A and B) and Temperature profile (C) for all three scenarios. Shaded area marks depth range for present-day smectite-illite transformation, below this area smectite-illite transformation is completed.

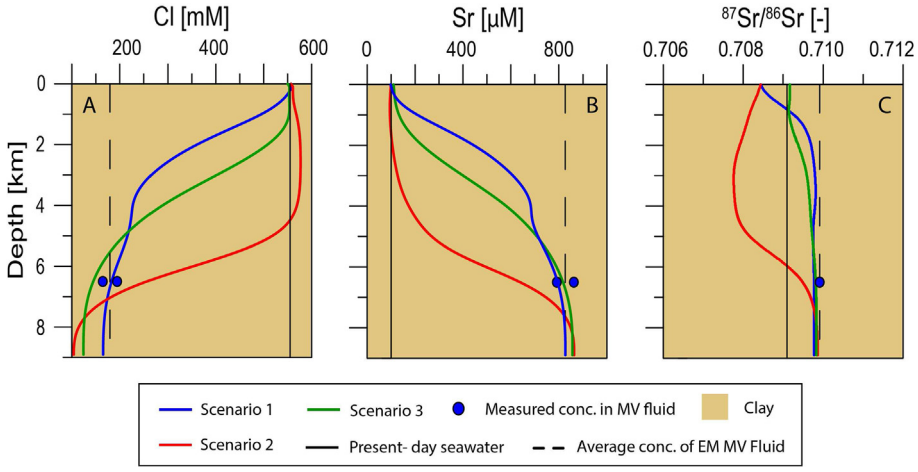

Fig. 4. Depth profiles of dissolved Cl (A), Sr (B) and $^{87}Sr/^{86}Sr$ (C) for CAMV. Measured concentrations are plotted in identified source depth. Black solid line is the average measured concentration of MV. Dashed line marks the modern seawater composition.

in the west for the GoC. However, applying only modern values to the time span of plate forming, this may cause an underestimation of the thermal state of the sediments, as at young crustal ages, the heat flow values may reach up to 300 mW m^{-2} (e.g. Stein and Stein, 1993). According to plate cooling models (e.g. Hasterok, 2013), the heat flow decreases fast at the beginning and reaches levels similar to modern heat flow values 50–60 Ma after plate formation. In the following, we test two variations for CAMV with (1) high heat flux of 300 mW m^{-2} in the beginning decreasing with time to present day heat flux, and (2) a constant heat flux 45 mW m^{-2} over time (Fig. 5) to see the impact of a high heat flow at the beginning of the model run time.

The fast decrease of heat flux from plate cooling models to a 135 Ma oceanic plate can be observed in Fig. 5, where the heat flow drops to a level of 45 mW m^{-2} after 55 Ma. Therefore, both tested scenarios have for at least the last 80 Ma of model run time a heat flow equivalent to the present one.

The temperature profile for the scenario with the elevated heat flow shows a positive temperature offset of up to 30 °C for the first 35 Ma compared to the low, constant heat flow scenario (Fig. 6). After 50–60 Ma, the difference between both scenarios is negligible. The higher temperature at the beginning results in an earlier dehydration of smectite. This causes a stronger decrease of Cl by up to 40 mM in the first 35 Ma of model run time (Fig. 6). However, with a decreasing smectite content also the rate of dehydration drops. Therefore, with the same amount of smectite transformed into illite at the end of the model run time, the effect of lower Cl values also disappears after ≈65 Ma. At this stage, the plate cooled down to its present-day heat flux. Hence, most of the sediments have likely not experienced a higher heat flow than 45–65 mW m^{-2}. As a consequence, and for simplicity, a constant heat flow over time has been chosen for all subsequent scenarios.

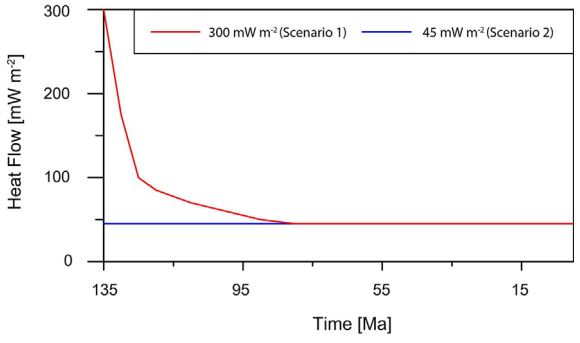

Fig. 5. Heat flow variations vs. time (Ma) for CAMV.

Overall, the implemented reaction transport module is able to simulate a fluid composition within the sedimentary units that is similar to the one at CAMV and other MVs on the accretionary wedge, reported by Scholz et al. (2009) and Hensen et al. (2015). The rate of clay-mineral dehydration could be constrained by the temperature distribution and key control factors from previous studies, resulting in a main reaction window between 50 and 150 °C as suggested by Cuadros and Linares (1996).

4.2. Case study 2: ATI MVs

The three ATI MVs are located in the south-eastern part of the Horseshoe Valley at a water depth of ~4500 m (Fig. 1). Emanating fluids of the MVs show a decrease of about 50 mM in Cl compared to modern seawater. Sr concentrations vary between 500 µM and 1000 µM, whereas the $^{87}Sr/^{86}Sr$ ratios are close to 0.7075 for all three MVs. According to Hensen et al. (2015), the two main processes affecting the fluid genesis are clay mineral dehydration and recrystallization of Upper Jurassic carbonates.

The sedimentary structure for the basin model of the ATI MVs is derived from multichannel seismic profile SW07 from the ESF funded SWIM cruise 2006 (Martínez-Loriente et al., 2013; Hensen et al., 2015). It consists of about ~1.3 km of Upper Jurassic carbonates followed by ~3.7 km of terrigenous sediments. The carbonates are underlain by oceanic crust, which has been formed during the Jurassic (Martínez-Loriente et al.,

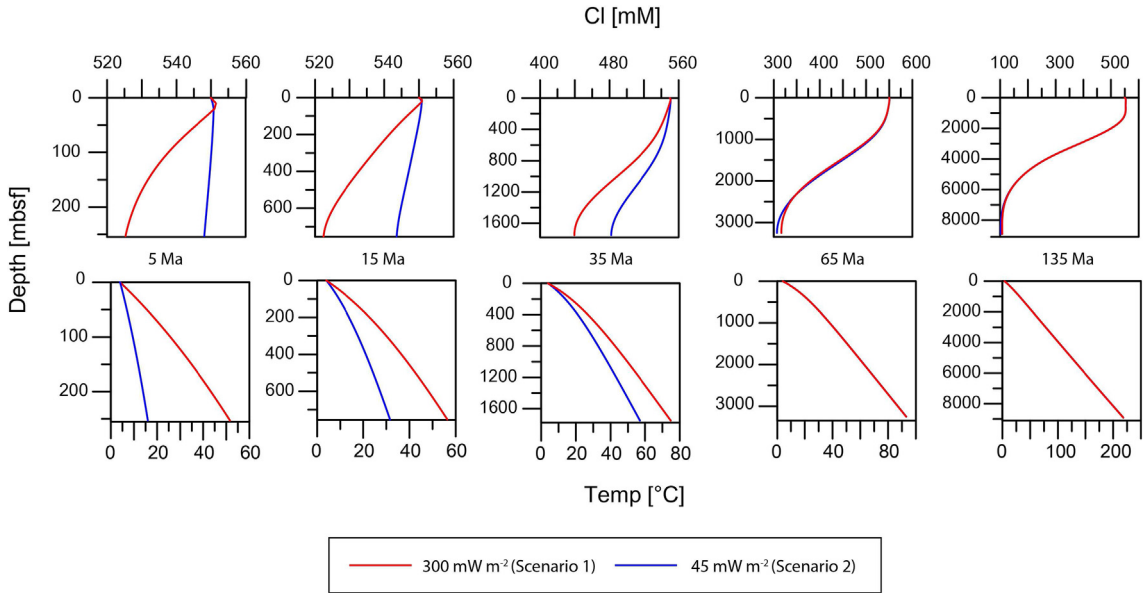

Fig. 6. Cl vs. depth and temperature vs. depth profiles for model runtime after 5 Ma, 15 Ma, 35 Ma, 65 Ma and 135 Ma for high heat flow (300 mW m^{-2}, Scenario 1) and constant heat flow (45 mW m^{-2}, Scenario 2) of CAMV.

2014) and are characterized by the low Sr isotope ratio reported for the Upper Jurassic. The overall run time for the model is set to 155 Ma, while during the first 30 Ma mainly carbonate with a small amount of clay (7.5 wt% smectite and 2.5 wt% illite) is deposited, the last 125–0 Ma are followed by a sequence of predominantly terrigenous clay sedimentation.

The numerical model approach of Richter and DePaolo (1987) for the recrystallization of carbonates has been used by other authors e.g. Richter and Liang (1993), Fantle and DePaolo (2006), and Fantle et al. (2010, 2015). The effective distribution coefficient K in Eq. (4), defined as the ratio of the Sr concentration in the carbonate, to the Sr concentration in fluid, is the most crucial parameter to control the reaction. Aforementioned authors typically used values between 12 and 20 for this parameter, derived from existing Sr^{2+} data of pore fluids and Sr concentrations of carbonates of ODP/IODP drill cores, while reported values for an effective distribution coefficient from experimental data range between <15 to >50 (Katz et al., 1972; Lorens, 1981). Since DSDP Site 135 did not reach the carbonate deposits there is no data set for the Sr content of carbonates in the working area. As a consequence, two values for K have been tested for the ATI MVs (Fig. 7).

During the recrystallization of carbonates no fresh water is released and hence, there is no effect on conservative elements by dilution. This explains why Cl concentration depth profiles for both scenarios are identical (Fig. 7A). The lower Cl concentration of about 495 mM at maximum depth compared to seawater (550 mM), results from a diffusive equilibration from the part of the model column where clay minerals are present. In this model section Cl shows a

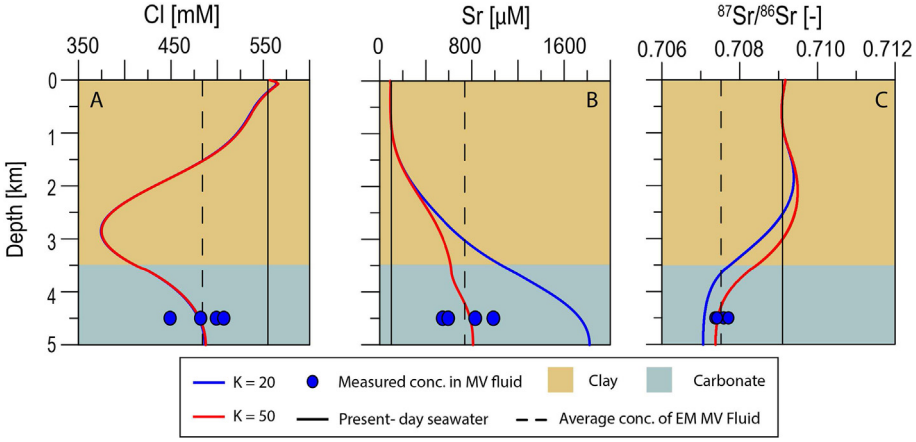

Fig. 7. Depth profiles of dissolved Cl (A), Sr (B) and $^{87}Sr/^{86}Sr$ (C) for ATI MVs with varying K values. Measured concentrations are plotted at the estimated source depth. Dashed line marks the modern seawater composition.

minimum of ~400 mM. The Cl values present in the part of carbonate sediments, are in the range of the observed emanating fluid composition of the MVs. Applying effective distribution coefficients of K = 20, results in Sr concentrations within the fluid of ~1850 µM (Fig. 7B). Concentrations above 1000 µM have not been observed, but the highest concentration measured is 978 µM and the large scatter of data implies that also higher concentrations are not unlikely. An effective distribution coefficient of 50 leads to Sr concentrations representing the average observed concentrations of emanating fluids in a depth range from 3.0 to 5.0 km.

The combination of a high isotopic ratio from the clay dehydration and a medium isotope ratio from the carbonate recrystallization, should lead to a ratio lying between the two sources. Both tested model scenarios are able to reproduce the observed isotopic ratios, where K = 20 leads to the lowest ratio and K = 50 to the highest ratio.

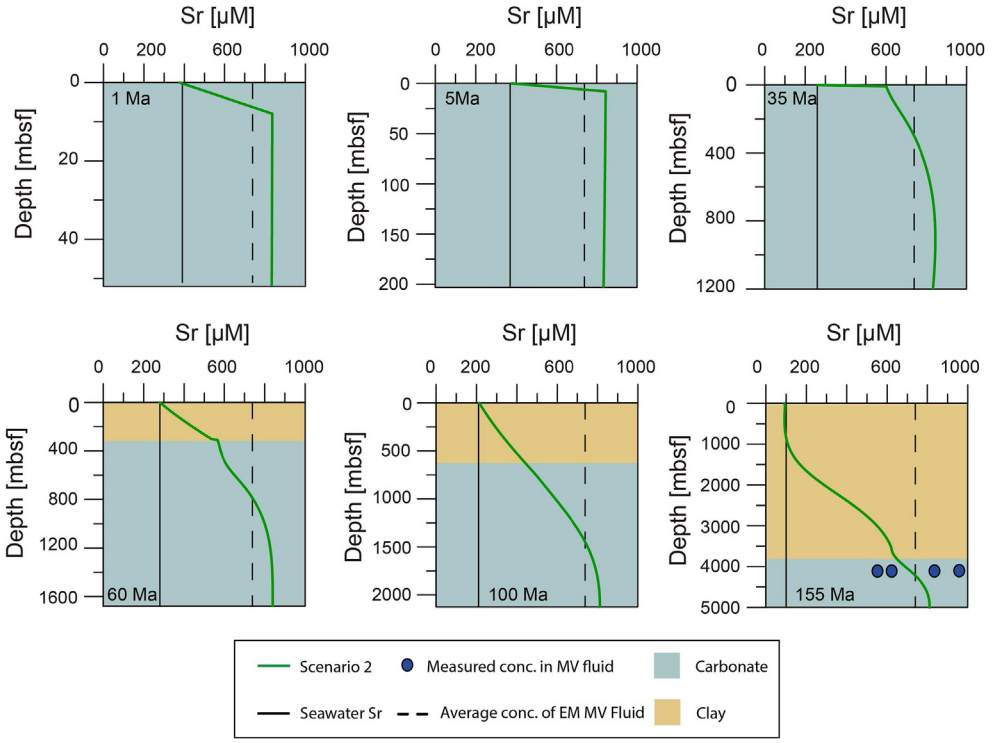

Fig. 8. Sr concentrations depth profiles for 6 time steps at 1 Ma, 5 Ma, 35 Ma, 60 Ma, 100 Ma and 155 Ma model run time, for third scenario of ATI MV with an effective distribution coefficient of 50. Dashed line is indicating the seawater Sr concentration for the point in time (see Fig. 2C). For the last time step the measured concentrations are plotted (blue points) at the estimated source depth.

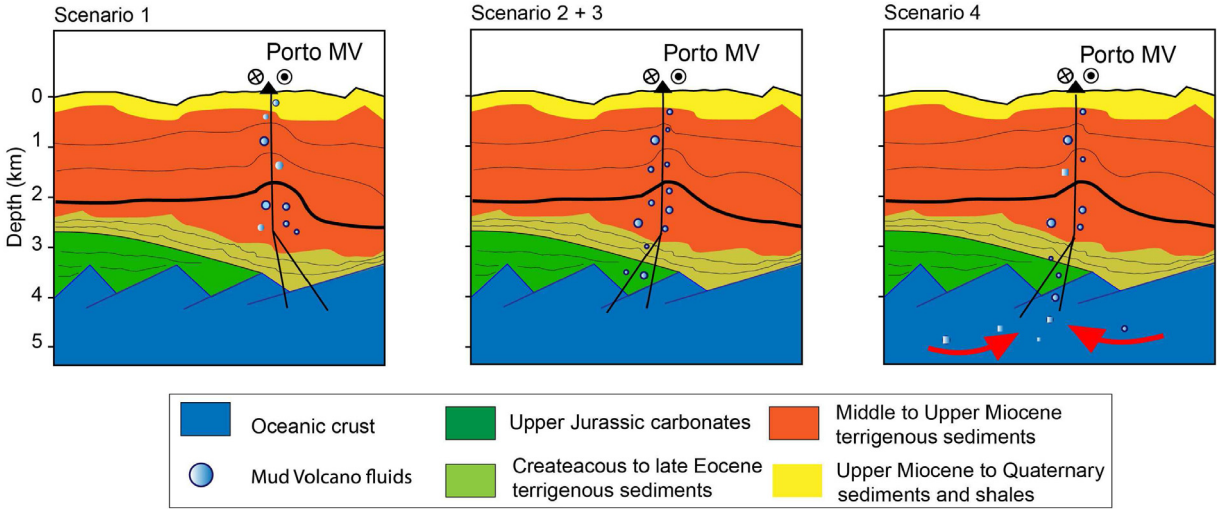

Fig. 9. Schematic sketches of the four scenarios tested for the Porto MV.

However, the variation between the scenarios is fairly small and the isotope ratio for all scenarios plots between 0.7070 and 0.7075 in the presumed source area (Fig. 7C).

Fig. 8 shows the Sr evolution over time for the second scenario of the ATI MVs. Reaction rates for recrystallization are highest right after deposition, the Sr concentration rises to about 850 μM in the lower part of the model domain within the first few million years. With ongoing sedimentation of terrigenous material, the Sr concentration decreases in the upper part of the modeling domain. Essentially, it becomes obvious that the major geochemical signal we see today in the emanating MV fluids has largely been formed shortly after the deposition of the carbonates.

4.3. Case study 3: Porto MV

Porto MV is located at the toe of the accretionary wedge at 3800 m water depth (Fig. 1) and shows the most complex combination of geochemical tracers investigated in this study. Endmember MV fluids are characterized by low Cl concentrations of 350 mM, Sr concentrations of about 400 μM, and a $^{87}Sr/^{86}Sr$ ratio of 0.7078.

Results of the first scenario (Fig. 9; sedimentation of terrigenous clay over 135 Ma forming a sedimentary column of ~3.8 km thickness) clearly indicate that the fluid composition, specifically the $^{87}Sr/^{86}Sr$ ratio (Fig. 10C), cannot be explained by smectite to illite transformation only. An

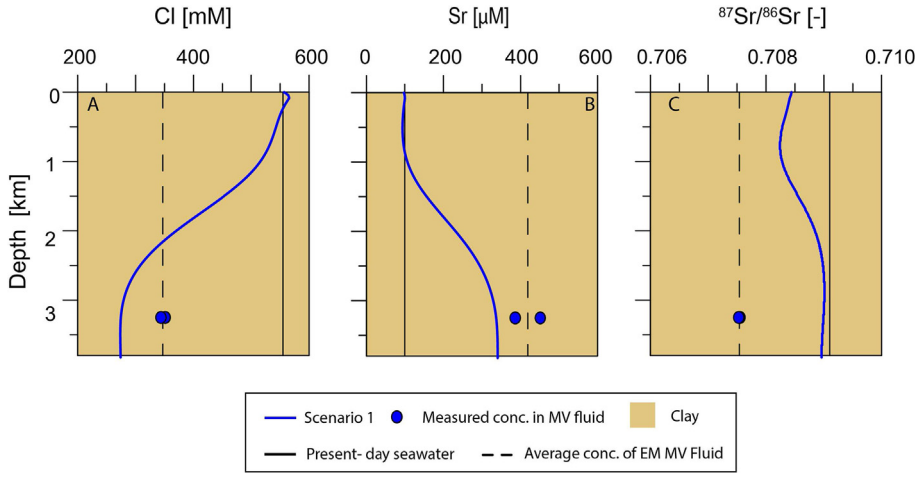

Fig. 10. Depth profiles of dissolved Cl (A), Sr (B) and $^{87}Sr/^{86}Sr$ (C) for the first scenario of Porto MV. Measured concentrations are plotted at the estimated source depth of MV fluids. Dashed line marks the modern seawater composition.

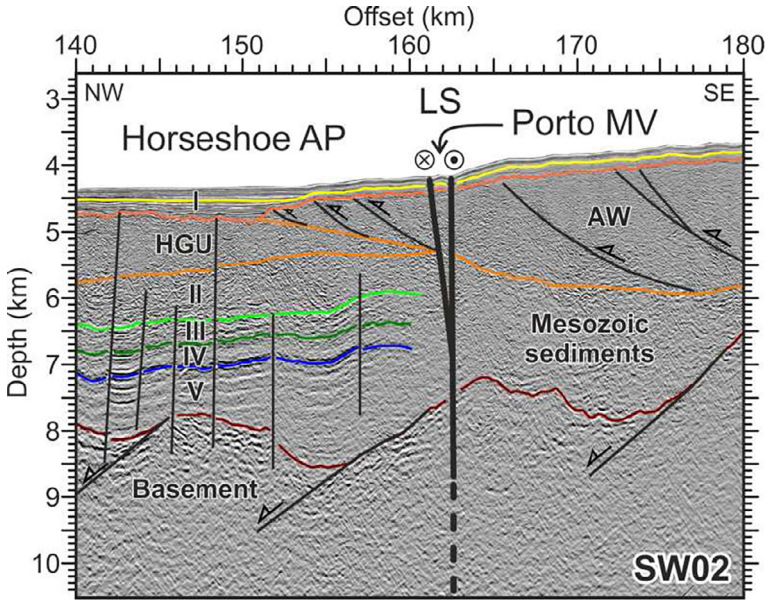

Fig. 11. Stratigraphic interpretation of pre-stack depth migrated multichannel seismic profile SW02 crossing Porto MV (modified from Martínez-Loriente et al., 2018). AW: Accretionary wedge, LS: Lineament South; HGU: Horseshoe gravitational unit; I: Upper Oligocene to Quaternary; II: Upper Cretaceous to Lower Eocene; III: Cretaceous; IV: Lower Cretaceous; V: Upper Jurassic. See Fig. 1 for location.

additional Sr source with a low to medium isotope ratio (e.g. from carbonate recrystallization as considered in case study 2) is required to obtain a better fit. Previously, Hensen et al. (2015) suggested that Upper Jurassic carbonates are absent in this area. However, Martínez-Loriente et al. (2018) showed that the area is marked by a number of horst and graben structures, which are illustrated by a depth-migrated seismic line crossing Porto MV (Fig. 11). According to the stratigraphic interpretation, Upper Jurassic carbonates may be present to some extent in the graben structures northwest of Porto MV (kilometre 140–160 in seismic profile SW02). Southeast of Porto there is no evidence for the existence of Upper Jurassic carbonates; sediments there are generally of Mesozoic age and their composition cannot be clearly identified.

Based on this evidence, we tested two scenarios explicitly considering carbonate recrystallization occurring in carbonate layers of about 240 m (Fig. 12A–C) and 670 m (Fig. 12D–F) thickness below the overlying ~3.6 km and 3.2 km of terrigenous sediments (Fig. 9). The run time was set to 155 Ma considering the longer time of sediment deposition since the Upper Jurassic. The results show that a relatively thin layer of carbonate is not sufficient to obtain an acceptable fit to the data (Scenario 2). Recrystallization rates result in a good fit to the Sr concentrations (Fig. 12B), although fail to obtain sufficiently low $^{87}Sr/^{86}Sr$ ratios

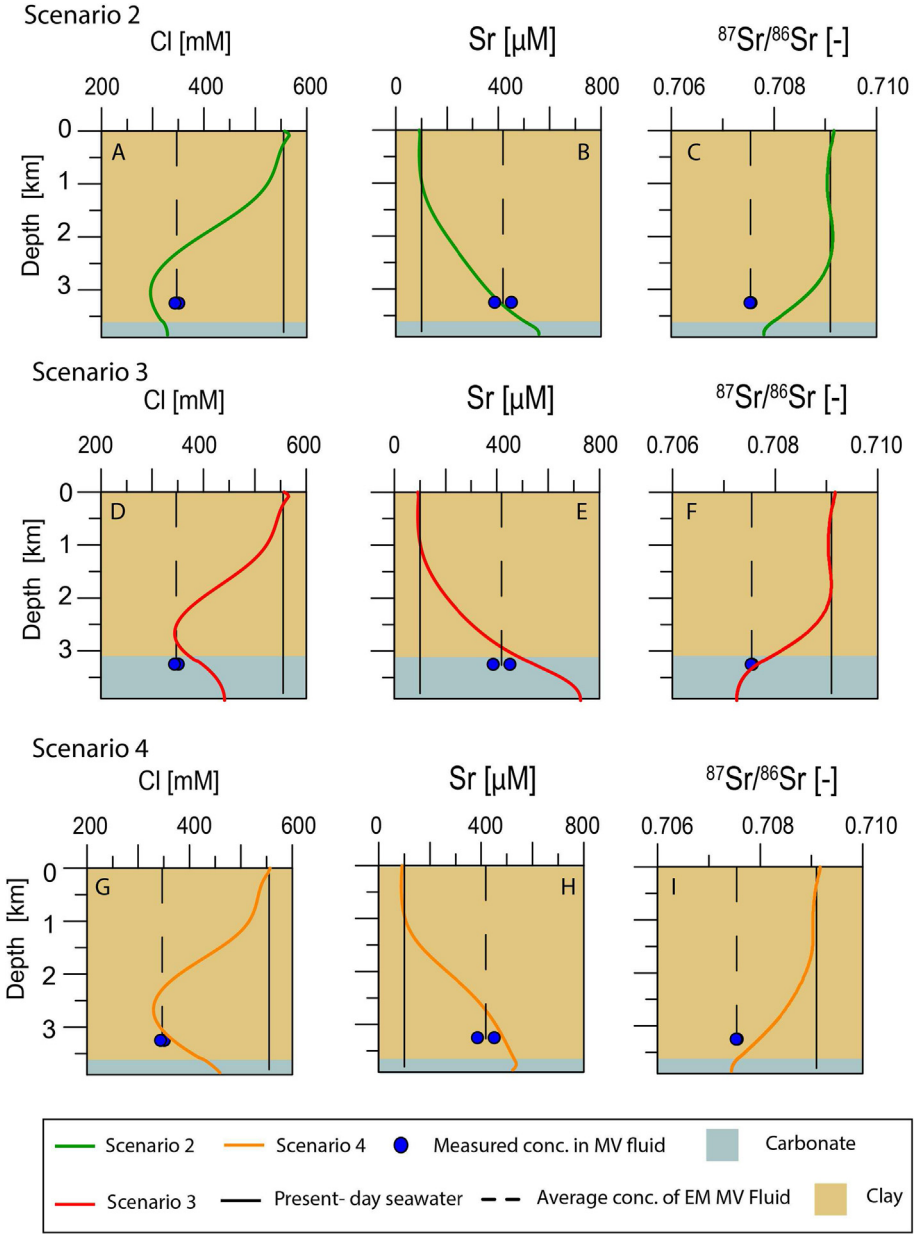

Fig. 12. Depth profiles for solutes Cl and Sr and isotope ratio of $^{87}Sr/^{86}Sr$, for second (A–C), third (D–F) and fourth (G–I) scenarios of Porto MV. Measured concentration is plotted in the estimated source depth. Dashed line marks the modern seawater composition.

(Fig. 12C). Vice versa, enhanced carbonate recrystallization due to a thick carbonate layer (Scenario 3) result in a good fit to the data with only slightly over-predicted Sr concentrations (Fig. 12E). However, the evidence for the existence of thick carbonate deposits at this location is weak. Generally, the alteration of mafic materials like volcanic ash is known to create low isotopic $^{87}Sr/^{86}Sr$ ratios in pore fluids. However, such deposits have not been reported for the GoC (Scholz et al., 2009). Alternatively, admixing of fluids from the underlying oceanic crust has been proposed (Scholz et al., 2009; Hensen et al., 2015). Although such a scenario remains speculative as the precise mechanism and the driving force for an upward advection are currently not known, we simulated such hypothetic injection into basal sediments (for about 30 Ma years) assuming concentrations and isotope values of crustal fluids as detailed in Section 3.3. In addition to the smectite to illite transformation in the terrigenous section, we combined carbonate recrystallization within a carbonate layer of 240 m thickness and the injection of fluids from the oceanic crust (Fig. 9). With this combination of parameters, we also achieved a good approximation to the measured MV endmember data (Fig. 12G–I), with a predicted source area of the MV fluids located above the carbonate sequence at roughly 3.25 km sediment depth. Assuming fluid advection through aged oceanic crust, major unknown parameters are the onset and the velocity of the flow. For our hypothetic scenario, we assume that it is related to the onset of subduction of the oceanic crust beneath the Gibraltar Arc, which started in the Tortonian (e.g. Duarte et al., 2013). Interestingly, mud volcanism in the GoC is reported to occur since the Mid-Tortonian (Toyos et al., 2016). The continuing convergence of the Eurasian and African plates could have provided the development of suitable conditions for focussed fluid advection, for example the opening of permeable fault systems. Analogously, the existence of MVs in front of the Barbados accretionary wedge has been ascribed to the reorganization of the fluid-flow regime in the igneous oceanic crust due to the change of tectonic stress along a fracture zone (see Section 4.4; Sumner and Westbrook, 2001).

It must be admitted at this stage that a sufficient pressure gradient leading to the upward advection of fluids from the oceanic crust can likely only be assumed along deep-reaching high permeability zones such as the LS fault (Figs. 1 and 11). However, a fully appropriate simulation of such a scenario would require at least a 2D model approach, which is beyond the scope of the present study. Nevertheless, the results of our simplified model approach show that the injection of crustal-derived fluids offers a potential explanation for the observed fluid composition at Porto MV. In addition, the existence of such a transport pathway provides also a general mechanism to mobilize fluids from the oldest carbonate units deposited on top of the basement, since in situ fluid mobilization in such sediments is unlikely to occur.

4.4. Summary of case studies

Overall, all three case studies reveal that the numerical approach is appropriate to reproduce measured endmember concentrations of MV fluids at certain subsurface depth levels, indicating possible source regions of the fluids. The simulation results of all case studies are summarized together with fluid endmember data from respective mud volcanoes in cross plots of Cl vs Sr and $^{87}Sr/^{86}Sr$ in Fig. 13, where the simulated data point always represents the concentration in the depth horizon with the closest match to the data. For the CAMV case study the best fit was obtained at 6.5 km (Fig. 4), for ATI at 4.5 km (Fig. 7), and for Porto at 3.25 km sediment depth (Fig. 12). Generally, these results confirm previously made, but less constrained, estimates of the source depths of fluids or their approximate stratigraphic origin (e.g. Pinheiro et al., 2005; Hensen et al., 2007, 2015; Scholz et al., 2009).

The source depth of fluids decreases to the west and seems to be correlated with the total sediment thickness (Gutscher et al., 2009), which is a rough indicator for the potential of producing low-salinity fluids by clay-mineral dehydration (Scholz et al., 2010b), being one of the major processes driving fluid advection and mud volcanism on the accretionary wedge. Analogously, this may imply

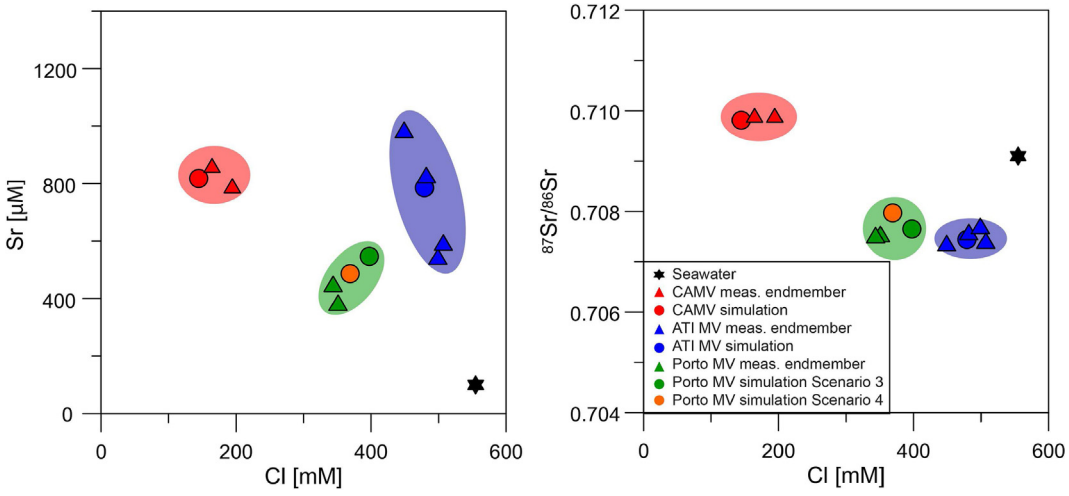

Fig. 13. Endmember plots of measured vs. modeled data; A: Cl vs Sr. B: Cl vs. $^{87}Sr/^{86}Sr$.

that – due to the reduced potential of clay-mineral dehydration below the distal mud volcanoes – other process like fluid flow through the oceanic crust (as discussed for the Porto case study) might be necessary to initiate mud volcanism in this area. The predicted source depth in the ATI case study and Porto scenario 4 is located within the Upper Jurassic carbonates. As indicated above, carbonate recrystallization is a process affecting the fluid composition, but not generating fluids. Hence, also in the ATI area fluid injection from the oceanic basement might stimulate fluid flow and by this capturing chemical signals even from the oldest sedimentary strata above the basement (cf. Hensen et al., 2015).

Interestingly, the mechanisms described above do not seem to represent an isolated, special case only, but can be considered of being of broader significance. Deep-seated fluids expelled at MVs located offshore the deformation front of the Barbados Accretionary Prism have been generally ascribed to be the result of dewatering processes occurring in the subducting slab sediments and migrating upward along major fault systems such as the décollement (e.g. Dia et al., 1995; Godon et al., 2004). However, a closer look at the geotectonic setting shows a close analogy to the situation observed in the Gulf of Cadiz. Similar to ATI MVs and Porto MV being aligned along the LS fault, Barbados MVs are aligned parallel to the Mercurus Fracture Zone in front of the accretionary prism. Sumner and Westbrook (2001) alternatively suggested that mud volcanism in this area was initiated by changes in plate motion along this fracture zone and driven by water released by the smectite to illite transformation affected by the circulation of fluids in the oceanic crust. Altogether, these observations call for a reassessment of previously made conclusions on fluid sources of the Barbados MVs and, in general, a closer investigation of the potential fluid flow in aged oceanic crust (>65 Ma). Numerical modeling as presented in this study may play a key role to identify and quantify major physical and geochemical processes involved.

5. CONCLUSIONS AND IMPLICATIONS

With our novel, fully-coupled, basin-scale model approach, we are able to simulate ubiquitous fluid forming processes, largely affecting the pore water geochemistry in deeply buried marine sedimentary environments. Using fluid data from MVs in the GoC we were able to constrain reaction rates and source depths of fluid generation. In summary, the most important aspects are:

- The numerical model approach is able to reproduce fluid signatures that have been observed in MV fluids on the upper continental slope and the deep sedimentary basin.
- Clay dehydration results in the dilution of conservative elements and the enrichment of fluid mobile Sr with radiogenic $^{87}Sr/^{86}Sr$ ratios. Carbonate recrystallization produces Sr enriched fluids with a distinct $^{87}Sr/^{86}Sr$ ratio shortly after the deposition of carbonates. With these reactions most of the fluid compositions measured at MVs within the GoC can be described satisfactorily and approximate source depths can be assigned.
- Fluid injection from the basement as suggested by Hensen et al. (2015) might play a role at the distant MVs in order to explain the geochemical signature at Porto MV and more generally, as a mechanism of mobilizing pore water from the oldest strata above the basement.

Overall, we were able to substantiate previously made conventional geochemical interpretations and the understanding of fluid genesis in the area. This novel model approach provides a powerful tool to analyse fluid generation and geochemical processes in sedimentary basins and is easily transferable to other regions and geochemical systems. Future models of this type will be expanded to 2D to enable adequate simulations of fluid generation and potential advection along low-permeability conduits. Finally, analogies to observations at the Barbados accretionary margin imply that fluid circulation in old oceanic crust – in combination with the occurrence of strike-slip fault systems and fracture zones – is a process with currently unknown importance to fluid dynamics and element cycling in sedimentary systems, which deserves systematic investigation in the future.

The authors declare that they have no conflict of interest.

ACKNOWLEDGEMENTS

The manuscript benefited from additional support by the project FLOWS (EU-COST Action 1301). Project CTM2015-70155-R (INSIGHT) has been funded through the Spanish Ministry of Science and Innovation. The manuscript benefited from constructive reviews of A. Mazzini, J. Ishibashi and an anonymous reviewer.

APPENDIX A

A.1 Governing equations

The 1D model used for this study is based on the assumption that the pore space is fully saturated by fluids. Sediment grains and fluids are transported downwards according to the burial velocity. The burial velocity of solids is derived from the sedimentation rate from DSDP Site 135 on Coral Patch Ridge (Hayes et al., 1972). The mass balance for solids reads as follows:

$$\frac{\partial((1-\Phi)\rho_s)}{\partial t} = -\nabla \cdot ((1-\phi)\rho_s \overrightarrow{V_s}) + Q_s \quad \text{(A1)}$$

where ϕ – porosity, ρ_s – solid density, V_s – burial velocity of solids, t – time and Q_s – source term for mineral reactions.

The mass balance for fluids reads as follows:

$$\frac{\partial(\phi\rho_f)}{\partial t} = -\nabla \cdot (\phi\rho_f \overrightarrow{V_f}) + Q_f \quad \text{(A2)}$$

where ρ_f – fluid density, V_f – fluid phase velocity and Q_f – source term for biogeochemical reactions in the fluid phase.

Concentrations of dissolved species are transported by diffusion and advection after following equation:

$$\frac{\partial(\phi C)}{\partial t} = -\nabla \cdot (\phi D_s \nabla C) - \nabla \cdot (\phi\ C\ \overrightarrow{V_f}) + Q_{fc} \quad \text{(A3)}$$

where C – concentration of solutes, D_s – diffusion coefficient, and Q_{fc} – source term for biogeochemical reactions of each chemical species in the fluid phase. Fluid velocity V_f was calculated after the Darcy formulation which reads as

$$\overrightarrow{U_f} = \phi(\overrightarrow{V_f} - \overrightarrow{V_s}) = -\frac{k}{\mu_f}(\nabla P - \rho_f\ \overrightarrow{g}) \quad \text{(A4)}$$

where U_f – Darcy fluid velocity, k – intrinsic permeability, μ_f – viscosity of fluid phase, ∇P – pressure gradient, and g – gravitational acceleration. The viscosity of fluids depends on temperature and pressure, however, here we used a constant average value (see Table A1).

The temperature-dependent molecular diffusion coefficients of dissolved species in the fluid are calculated according to Boudreau (1997). The diffusion coefficient D_s is the molecular diffusion coefficient scaled by the tortuosity, which is calculated using the following equation (Boudreau 1997):

$$T_o = 1 - 2 \cdot \log(\phi) \quad \text{(A5)}$$

The intrinsic permeability can be derived with the Kozeny-Carman relation. This relationship is defined after Hantschel and Kauerauf (2009) as:

$$k = \frac{B \cdot \phi^3}{T_o^2 \cdot S^2} \quad \text{(A6)}$$

where B – is the scaling factor and S – is the specific sediment surface area. Values for S and B that are applied to characterize the permeability of the GoC lithologies are based on Hantschel and Kauerauf (2009) (Table A1).

Pressure equations

The lithostatic pressure, assuming a constant sediment grain density, has been calculated according to following equation after Hantschel and Kauerauf (2009)

$$P_{Litho_{(z)}} = \rho_{seawater} \cdot g \cdot wd + P_{Aero} + g \cdot \int_{z_0}^{z} (\rho_f \phi + \rho_s(1-\phi)) d_z \quad \text{(A7)}$$

where P_{Litho} – lithostatic pressure, $\rho_{seawater}$ – seawater density, wd – water depth, P_{Aero} – atmospheric pressure, z_0 – seafloor and z – sediment depth.

The effective pore fluid pressure P calculation is based on the Terzaghi's effective stress definition and accounts for compressible fluids and incompressible grains. P is calculated according to the following equation:

$$\rho_f(\phi\beta_f + \frac{\varsigma}{(1-\phi)})\frac{\partial P}{\partial t} - \nabla \cdot (\frac{\rho_f k}{\mu_f}\nabla P) = \nabla \cdot (\frac{\rho_f k}{\mu_f}(\rho_f\ \overrightarrow{g})) + \frac{\rho_f \varsigma}{(1-\phi)}\frac{\partial P_{Litho}}{\partial t} - \frac{\partial \rho_f}{\partial t} + Q_{Reaction} \quad \text{(A8)}$$

where β_f – compressibility factor for fluids, ς – sediment compaction parameter, P the effective pore fluid pressure, and $Q_{Reaction}$ source term for pore fluid released from chemical reactions.

Table A1
Parameters used in the governing equations of the basin model.

Parameter	Symbol	Value	References
Gravitational acceleration	g	9.81 m s^{-2}	–
Time step	dt	200,000 years	–
Density of solids	ρ_s	2600 kg m^{-3}	–
Density of fluids	ρ_f	1000 kg m^{-3}	–
Geometrical factor	B	10	Based on Hantschel and Kauerauf (2009)
Specific surface area	S	10^5 m^2 m^{-3}	Based on Hantschel and Kauerauf (2009)
Dynamic viscosity of fluid	μ_f	10^{-3} Pa s	Xu and Germanovich (2006)
Thermal conductivity of solids	λ_s	2.0 W m^{-1} K^{-1}	Hantschel and Kauerauf (2009)
Thermal conductivity of fluid	λ_f	0.6 W m^{-1} K^{-1}	Hantschel and Kauerauf (2009)
Specific heat capacity of solids	$C_{ps(clay)}$	940 J kg^{-1} K^{-1}	Hantschel and Kauerauf (2009)
	$C_{ps(carbonate)}$	840 J kg^{-1} K^{-1}	Hantschel and Kauerauf (2009)
Specific heat capacity of fluid	C_{pf}	4181.3 J kg^{-1} K^{-1}	Hantschel and Kauerauf (2009)
Sedimentation rate of solids 155–120 Ma	$V_{S\ 155–120\ Ma}$	55 m Ma^{-1}	Modified after Hayes et al. (1972)
Sedimentation rate of solids 120–25 Ma	$V_{S\ 120–25\ Ma}$	25 m Ma^{-1}	Modified after Hayes et al. (1972)
Sedimentation rate of solids 25–0 Ma	$V_{S\ 25–0\ Ma}$	150 m Ma^{-1}	Modified after Hayes et al. (1972)
Seawater temperature	T_0	4 °C	–
Atmospheric pressure	P_{aero}	101,325 Pa	–
Compressibility of fluid	β_f	$4 \cdot 10^{-10}$ Pa^{-1}	Hantschel and Kauerauf (2009)
Initial porosity	$\phi_{0(clay)}$	0.6	Hantschel and Kauerauf (2009)
	$\phi_{0(carbonate)}$	0.5	Hantschel and Kauerauf (2009)
Sediment compaction parameter	ς_{clay}	$1.7 \cdot 10^{-7}$ Pa^{-1}	Hantschel and Kauerauf (2009)
	$\varsigma_{carbonate}$	1.176 10^{-7} Pa^{-1}	Hantschel and Kauerauf (2009)
Intrinsic permeability	k	Eq. (A6)	Hantschel and Kauerauf (2009)

The first term on the LHS of the pore pressure Eq. (A8) accounts for a density change of fluid with time. A compressibility factor for fluids (β_f) is calculated as:

$$\beta_f \rho_f = \frac{\partial \rho_f}{\partial P} \tag{A9}$$

The first term on the RHS accounts for mobility of a fluid due to the pressure change and gravitational flow. The second last term on the RHS, the volume expansion term, describes changes in fluid density with time, and the last term is the source term.

The effective stress calculation is used to estimate the porosity reduction due to sediment compaction. Thus, the actual state of the pore fluid pressure P is used to calculate the amount of pore fluids expelled from the matrix. The effective stress reads as follows:

$$\sigma'_z = P_{Litho} - P \tag{A10}$$

where $\dot{\sigma_z}$ – the effective stress. The porosity is calculated after modified Athy's law taking into account the effective stress:

$$\phi = \phi_{res} + \phi_0 e^{-\varsigma \sigma'_z} \tag{A11}$$

where ϕ_{res} – residual porosity, ϕ_0 – initial porosity. The residual porosity stands for the irreducible fraction of the pore space filled by pore fluids.

Temperature

The temperature field is determined using an average constant basement heat flow over time, and constant sediment water interface temperature (T_0). Heat is transported via advection and diffusion in the model domain. The temperature distribution (T) reads as follows:

$$\frac{\partial}{\partial t}((\rho C_p)_{bulk} T) = -\nabla \cdot (((\rho C_p)_{bulk} \overrightarrow{V_s}) T) - \nabla \cdot ((\rho_f C_f \overrightarrow{U_f}) T) + \nabla \cdot (\lambda_{bulk} \nabla T) \tag{A12}$$

where $(\rho C_p)_{bulk}$ – volumetric heat capacity, C_{pf} – heat capacity of fluids, and λ_{bulk} – thermal conductivity.

The bulk volumetric heat capacity accounts for the solid and fluid phase and reads as follows:

$$(\rho C_p)_{bulk} = (1-\phi)\rho_s C_{\rho_s} + \phi \rho_f C_{\rho_f} \tag{A13}$$

where ρ_s – density and C_{ps} – heat capacity for solids, and respectively ρ_f and C_{pf} for fluids. The bulk thermal conductivity can be expressed after Deming and Chapman (1989) as

$$\lambda_{bulk} = \lambda_s^{1-\phi} \lambda_f^{\phi} \tag{A14}$$

where λ_s – average thermal conductivity for solids, and λ_f – fluid respectively. Here we used constant values for thermal conductivities for solids and species. A list of all input parameters is provided in Table A1.

APPENDIX B

Table B1.

Table B1
Parameter variations for case studies and scenarios.

	Clay dehydration							Carbonate recrystallization				Advection trough crust in kg s^{-1} m^{-2}
	Alpha	Beta	Frequency factor	Activation energy	$^{87}Sr/^{86}Sr$ of smectite	wt% water in smectite	Sr in smectite (X_{Sr})	Alpha	Beta	Gamma	K	Flow rate through LBC (5–0 Ma)
CAMV Parameter test												
Scenario 1	5	0.25	3.00E−10	20000	0.7100	22.5	0.4	–	–	–	–	–
Scenario 2	5	0.25	90	120000	0.7100	22.5	0.4	–	–	–	–	
Scenario 3	5	0.25	3.5e−8	38500	0.7100	22.5	0.4	–	–	–	–	
CAMV Heat flow test												
Scenario 1	5	0.25	3.50E−08	38500	0.7100	22.5	0.4	–	–	–	–	
Scenario 2	5	0.25	3.50E−08	38500	0.7100	22.5	0.4	–	–	–	–	
ATI MV												
Scenario 1	5	0.25	3.50E−08	38500	0.7100	22.5	0.4	1.00E−07	0.05	4	20	–
Scenario 2	5	0.25	3.50E−08	38500	0.7100	22.5	0.4	1.00E−07	0.05	4	50	–
Porto MV												
Scenario 1	5	0.25	3.50E−08	38500	0.7095	25.0	0.2	–	–	–	–	
Scenario 2	5	0.25	3.50E−08	38500	0.7095	25.0	0.2	1.00E−07	0.05	4	50	
Scenario 3	5	0.25	3.50E−08	38500	0.7095	25.0	0.2	1.00E−07	0.05	4	50	
Scenario 4	5	0.25	3.50E−08	38500	0.7095	25.0	0.2	1.00E−07	0.05	4	50	1.5E−04

REFERENCES

Argus D. F., Gordon R. G., Demets C. and Stein S. (1989) Closure of the Africa-Eurasia-North America plate motion circuit and tectonics of the Gloria fault. *J. Geophys. Res.* **94**, 5585–5602.

Baker P. A., Gieskes J. M. and Elderfield H. (1982) Diagenesis of carbonates in deep-sea sediments-evidence from SR/CA ratios and interstitial dissolved SR2+ data. *J. Sediment. Res.* **52**.

Baptista M. A., Heitor S., Miranda J. M., Miranda P. and Mendes Vitor L. (1988) The 1755 Lisbon tsunami; evaluation of the tsunami parameters. *J. Geodyn.* **25**, 143–157.

Bartolome R., Gràcia E., Stich D., Martínez-Loriente S., Klaeschen D., Mancilla F., Lo Iacono C., Dañobeitia J. J. and Zitellini N. (2012) Evidence for active strike-slip faulting along the Eurasia-Africa convergence zone: implications for seismic hazard in the southwest Iberian margin. *Geology* **40**, 495–498.

Boudreau B. P. (1997) *Diagenetic models and their implementation: modelling transport and reactions in aquatic sediments*. Springer, Berlin, Heidelberg, New York.

Brown K. M., Saffer D. M. and Bekins B. A. (2001) Smectite diagenesis, pore water freshening, and fluid flow at the toe of the Nankai wedge. *Earth Planet. Sci. Lett.* **194**, 97–109.

Calvert A. J. and Potts C. G. (1985) Seismic evidence for hydrothermally altered mantle beneath old crust in the Tydeman fracture zone. *Earth Planet. Sci. Lett.* **75**, 439–449.

Castellini D. G., Dickens G. R., Snyder G. T. and Ruppel C. D. (2006) Barium cycling in shallow sediment above active mud volcanoes in the Gulf of Mexico. *Chem. Geol.* **226**, 1–30.

Chamley H. and Debrabant P. (1984) Mineralogical and geochemical investigations of sediments on the Mazagan Plateau, Northwestern African Margin (Leg-79, Deep-Sea Drilling Project). *Init. Rep. Deep Sea Drill. Proj.* **79**, 497–508.

Chamley H., Debrabant P., Foulon J., d'Argoud G. G., Latouche C., Maillet N., Maillot H. and Sommer F. (1979) Mineralogy and geochemistry of Cretaceous and Cenozoic Atlantic sediments off the Iberian peninsula (Site 398, DSDP Leg 47B). *Init. Repts. DSDP* **47**, 429–449.

Chan L.-H. and Kastner M. (2000) Lithium isotopic compositions of pore fluids and sediments in the Costa Rica subduction zone: implications for fluid processes and sediment contribution to the arc volcanoes. *Earth Planet. Sci. Lett.* **183**, 275–290.

Charlou J. L., Donval J. P., Zitter T., Roy N., Jean-Baptiste P., Foucher J. P. and Woodside J. (2003) Evidence of methane venting and geochemistry of brines on mud volcanoes of the eastern Mediterranean Sea. *Deep Sea Res. Part I.* **50**, 941–958.

Cuadros J. (2006) Modeling of smectite illitization in burial diagenesis environments. *Geochim. Cosmochim. Acta* **70**, 4181–4195.

Cuadros J. and Linares J. (1996) Experimental kinetic study of the smectite-to-illite transformation. *Geochim. Cosmochim. Acta* **60**, 439–453.

Deming D. and Chapman D. S. (1989) Thermal histories and hydrocarbon generation- example from the Utah-Wyoming thrust belt. *AAPG Bull. – Am. Assoc. Petr. Geol.* **73**, 1455–1471.

Demicco R. V., Lowenstein T. K., Hardie L. A. and Spencer R. J. (2005) Model of seawater composition for the Phanerozoic. *Geology* **33**, 877–880.

Dia A. N., Castrec M., Boulègue J. and Boudou J. P. (1995) Major and trace element and Sr isotope constraints on fluid circulations in the Barbados accretionary complex. Part I: Fluid origin. *Earth Planet. Sci. Lett.* **134**, 69–85.

Douville E., Charlou J., Oelkers E., Bienvenu P., Colon C. J., Donval J., Fouquet Y., Prieur D. and Appriou P. (2002) The rainbow vent fluids (36 14′ N, MAR): the influence of ultramafic rocks and phase separation on trace metal content in Mid-Atlantic Ridge hydrothermal fluids. *Chem. Geol.* **184**, 37–48.

Duarte J. C., Rosas F. M., Terrinha P., Schellart W. P., Boutelier D., Gutscher M.-A. and Ribeiro A. (2013) Are subduction zones invading the Atlantic? Evidence from the southwest Iberia margin. *Geology* **41**, 839–842.

Fantle M. S. (2015) Calcium isotopic evidence for rapid recrystallization of bulk marine carbonates and implications for geochemical proxies. *Geochim. Cosmochim. Acta* **148**, 378–401.

Fantle M. S. and DePaolo D. J. (2006) Sr isotopes and pore fluid chemistry in carbonate sediment of the Ontong Java Plateau: calcite recrystallization rates and evidence for a rapid rise in seawater Mg over the last 10 million years. *Geochim. Cosmochim. Acta* **70**, 3883–3904.

Fantle M., Maher K. and DePaolo D. (2010) Isotopic approaches for quantifying the rates of marine burial diagenesis. *Rev. Geophys.* **48**.

Fehn U., Moran J. E., Snyder G. T., Muramatsu Y. (2007) The initial 129I/I ratio and the presence of "old" iodine in continental margins (manuscript).

Fisher A. T. and Von Herzen R. P. (2005) Models of hydrothermal circulation within 106 Ma seafloor: constraints on the vigor of fluid circulation and crustal properties, below the Madeira Abyssal Plain. *Geochem. Geophys., Geosyst.*, 6.

Fitts T. G. and Brown K. M. (1999) Stress-induced smectite dehydration: ramifications for patterns of freshening and fluid expulsion in the N. Barbados accretionary wedge. *Earth Planet. Sci. Lett.* **172**, 179–197.

Fukao Y. (1973) Thrust faulting at a lithospheric plate boundary Portugal earthquake of 1969. *Earth Planet. Sci. Lett.* **18**, 205–216.

Godon A., Jendrzejewski N., Castrec-Rouelle M., Dia A., Pineau F., Boulegue J. and Javoy M. (2004) Origin and evolution of fluids from mud volcanoes in the Barbados accretionary complex. *Geochim. Cosmochim. Acta* **68**, 2153–2165.

Gràcia E., Dañobeitia J., Verges J. and Bartolome R. (2003a) Crustal architecture and tectonic evolution of the Gulf of Cadiz (SW Iberian margin) at the convergence of the Eurasian and African plates. *Tectonics* **22**. https://doi.org/10.1029/2001TC901045.

Gràcia E., Danobeitia J. and Verges J.PARCIFAL-TEAM (2003b) Mapping active faults offshore Portugal (36°N-38°N): implications for seismic hazard assessment along the southwest Iberian margin. *Geology* **31**, 83–86.

Gràcia E., Vizcaino A., Escutia C., Asioli A., Rodes A., Pallas R., Garcia-Orellana J., Lebreiro S. and Goldfinger C. (2010) Holocene earthquake record offshore Portugal (SW Iberia): testing turbidite paleoseismology in a slow-convergence margin. *Quat. Sci. Rev.* **29**, 1156–1172.

Grevemeyer I., Kaul N. and Kopf A. (2009) Heat flow anomalies in the Gulf of Cadiz and off Cape San Vincente, Portugal. *Mar. Pet. Geol.* **26**, 795–804.

Gutscher M.-A., Dominguez S., Westbrook G. K., Le Roy P., Rosas F., Duarte J., Terrinha P., Miranda J., Graindorge D. and Gailler A. (2012) The Gibraltar subduction: a decade of new geophysical data. *Tectonophysics* **574**, 72–91.

Gutscher M.-A., Dominguez S., Westbrook G. K. and Leroy P. (2009) Deep structure, recent deformation and analog modeling of the Gulf of Cadiz accretionary wedge: implications for the 1755 Lisbon earthquake. *Tectonophysics* **475**, 85–97.

Hantschel T. and Kauerauf A. I. (2009) *Fundamentals of Basin and Petroleum Systems Modeling*. Springer Science & Business Media.

Haffert L., Haeckel M., Liebetrau V., Berndt C., Hensen C., Nuzzo M., Reitz A., Scholz F., Schönfeld J., Perez-Garcia C. and Weise S. M. (2013) Fluid evolution and authigenic mineral

paragenesis related to salt diapirism – the Mercator mud volcano in the Gulf of Cadiz. *Geochim. Cosmochim. Acta* **106**, 261–286.

Hasterok D. (2013) A heat flow based cooling model for tectonic plates. *Earth Planet. Sci. Lett.* **361**, 34–43.

Hayes D. E., Pimm A. C., Beckmann J. P., Benson W. E., Berger W. H., Roth P. H., Supko P. R. and von Rad U. (1972) Site 135, DSDP, Initial Reports U.S. Government Printing Office, Washington, D.C. pp. 15–48.

Hensen C., Wallmann K., Schmidt M., Ranero C. R. and Suess E. (2004) Fluid expulsion related to mud extrusion off Costa Rica continental margin – a window to the subducting slab. *Geology* **32**, 201–204.

Hensen C., Nuzzo M., Hornibrook E., Pinheiro L. M., Bock B., Magalhães V. H. and Brückmann W. (2007) Sources of mud volcano fluids in the Gulf of Cadiz – indications for hydrothermal imprint. *Geochim. Cosmochim. Acta* **71**, 1232–1248.

Hensen C., Scholz F., Nuzzo M., Valadares V., Gràcia E., Terrinha P., Liebetrau V., Kaul N., Silva S., Martínez-Loriente S., Bartolome R., Piñero E., Magalhães V. H., Schmidt M., Weise S. M., Cunha M., Hilario A., Perea H., Rovelli L. and Lackschewitz K. (2015) Strike-slip faults mediate the rise of crustal-derived fluids and mud volcanism in the deep sea. *Geology* **43**, 339–342.

Hoefs J. (2004) *Stable Isotope Geochemistry*, fifth ed. Springer-Verlag, Berlin Heidelberg.

Hollister C. D., Ewing J. I., Habib D., Hathaway J. C., Lancelot Y., Luterbacher H., Paulus F. J., Poag C. W., Wilcoxon J. A. and Worstell P. (1972) Site 105 – Lower continental rise hills, Deep Sea Drilling Program, Initial Reports Washington, D.C. pp. 219–312.

Horita J., Zimmermann H. and Holland H. D. (2002) Chemical evolution of seawater during the Phanerozoic: implications from the record of marine evaporites. *Geochim. Cosmochim. Acta* **66**, 3733–3756.

Huang W.-L., Longo J. M. and Pevear D. R. (1993) An experimentally derived kinetic model for smectite-to-illite conversion and its use as a geothermometer. *Clays Clay Miner.* **41**, 162–177.

Kastner M., Elderfield H. and Martin J. B. (1991) Fluids in convergent margins: what do we know about their composition, origin, and role in diagenesis and importance for oceanic chemical fluxes? *Phil. Trans. R. Soc. London Ser. A* **335**, 243–259.

Katz A., Sass E., Starinsky A. and Holland H. (1972) Strontium behavior in the aragonite-calcite transformation: an experimental study at 40–98 C. *Geochim. Cosmochim. Acta* **36**, 481–496.

Kopf A. (2002) Significance of mud volcanism. *Rev. Geophys.* **40**, 1–52.

Kopf A. (2003) Global methane emission through mud volcanoes and its past and present impact on the Earth's climate. *Int. J. Earth Sci.* **92**, 806–816.

Lonergan L. and White N. (1997) Origin of the Betic-Rif mountain belt. *Tectonics* **16**, 504–522.

Lorens R. B. (1981) Sr, Cd, Mn and Co distribution coefficients in calcite as a function of calcite precipitation rate. *Geochim. Cosmochim. Acta* **45**, 553–561.

Luff R. and Wallmann K. (2003) Fluid flow, methane fluxes, carbonate precipitation and biogeochemical turnover in gas hydrate-bearing sediments at Hydrate Ridge, Cascadia Margin: numerical modeling and mass balances. *Geochim. Cosmochim. Acta* **67**, 3403–3421.

Maldonado A., Somoza L. and Pallares L. (1999) The Betic orogen and the Iberian-African boundary in the Gulf of cadiz: geological evolution (central North Atlantic). *Mar. Geol.* **155**, 9–43.

Martin J. B., Kastner M. and Elderfield H. (1991) Lithium: sources in pore fluids of Peru slope sediments and implications for oceanic fluxes. *Mar. Geol.* **102**, 281–292.

Martin J. B., Gieskes J. M., Torres M. and Kastner M. (1993) Bromine and iodine in Peru margin sediments and pore fluids: implications for fluid origins. *Geochim. Cosmochim. Acta* **57**, 4377–4389.

Martin J. B., Kastner M., Henry P., Le Pichon X. and Lallement S. (1996) Chemical and isotopic evidence for sources of fluids in a mud volcano field seaward of the Barbados accretionary wedge. *J. Geophys. Res.* **101**, 20325–20345.

Martínez-Loriente S., Gràcia E., Bartolome R., Sallarès V., Connors C., Perea H., Lo Iacono C., Klaeschen D., Terrinha P., Dañobeitia J. J. and Zitellini N. (2013) Active deformation in old oceanic lithosphere and significance for earthquake hazard: seismic imaging of the Coral Patch Ridge area and neighboring abyssal plains (SW Iberian Margin). *Geochem. Geophys. Geosyst.*, 14.

Martínez-Loriente S., Sallarès V., Gràcia E., Bartolome R., Dañobeitia J. J. and Zitellini N. (2014) Seismic and gravity constraints on the nature of the basement in the Africa-Eurasia plate boundary: new insights for the geodynamic evolution of the SW Iberian margin. *J. Geophys. Res. Solid Earth* **119**, 127–149.

Martínez-Loriente S., Gràcia E., Bartolome R., Perea H., Klaeschen D., Dañobeitia J. J., Zitellini N., Wynn R. B. and Masson D. G. (2018) Morphostructure, tectono-sedimentary evolution and seismic potential of the Horseshoe Fault, SW Iberian Margin. *Basin Res.* **30**, 382–400.

Mazzini A. and Etiope G. (2017) Mud volcanism: an updated review. *Earth Sci. Rev.* **168**, 81–112.

Mazzini A., Scholz F., Svensen H., Hensen C. and Hadi S. (2017) The geochemistry and origin of the hydrothermal water erupted at Lusi, Indonesia. *Mar. Petrol. Geol.*.

McArthur J. M., Howarth R. J. and Bailey T. R. (2001) Strontium isotope stratigraphy: LOWESS version 3: best fit to the marine Sr-isotope curve for 0–509 Ma and accompanying look-up table for deriving numerical age. *J. Geol.* **109**, 155–170.

Medialdea T., Somoza L., Pinheiro L. M., Fernandez-Puga M. C., Vazquez J. T., Leon R., Ivanov M. K., Magalhaes V., Diaz-del-Rio V. and Vegas R. (2009) Tectonics and mud volcano development in the Gulf of Cadiz. *Mar. Geol.* **261**, 48–63.

Milkov A. V. (2000) Worldwide distribution of submarine mud volcanoes and associated gas hydrates. *Mar. Geol.* **167**, 29–42.

Milkov A. V., Sassen R., Apanasovich T. V. and Dadashev F. G. (2003) Global gas flux from mud volcanoes: a significant source of fossil mathane in the atmosphere and the ocean. *Geophys. Res. Lett.* **30**, 1037, doi:1010.1029/2002GL016358.

Morse J. W. and Casey W. H. (1988) Ostwald processes and mineral paragenesis in sediments. *Am. J. Sci.* **288**, 537–560.

Morse J. W. and Mackenzie F. T. (1990) *Geochemistry of Sedimentary Carbonates*. Elsevier.

Nuzzo M., Hornibrook E. R. C., Gill F., Hensen C., Pancost R. D., Haeckel M., Reitz A., Scholz F., Magalhães V. H., Brückmann W. and Pinheiro L. M. (2009) Origin of light volatile hydrocarbon gases in mud volcano fluids, Gulf of Cadiz – evidence for multiple sources and transport mechanisms in active sedimentary wedges. *Chem. Geol.* **266**, 359–372.

Paull C. K., Dallimore S. R., Caress D. W., Gwiazda R., Melling H., Riedel M., Jin Y. K., Hong J. K., Kim Y. G., Graves D., Sherman A., Lundsten E., Anderson K., Lundsten L., Villinger H., Kopf A., Johnson S. B., Clarke J. H., Blasco S., Conway K., Neelands P., Thomas H. and Cote M. (2015) Active mud volcanoes on the continental slope of the Canadian Beaufort Sea. *Geochem. Geophys. Geosyst.* **16**, 3160–3181.

Pinheiro L. M., Ivanov M. K., Sautkin A., Akhmanov G., Magalhaes V. H., Volkonskaya A., Monteiro J. H., Somoza L., Gardner J. V., Hamouni N. and Cunha M. R. (2003) Mud volcanism in the Gulf of Cadiz: results from the TTR-10 cruise. *Mar. Geol.* **195**, 131–151.

Pinheiro L. M., Ivanov M., Kenyon N., Magalhães V. H., Somoza L., Gardner J. M., Kopf A., Van Rensbergen P., Monteiro J. H. and Euromargins-MVSEIS-Team (2005) Structural control of mud volcanism and hydrocarbon-rich fluid seepage in the Gulf of Cadiz: results from the TTR-15 and other previous cruises. CIESM Workshop Monograph. pp. 53–58.

Pytte A. M. and Reynolds R. C. (1989) The thermal transformation of smectite to illite. In *Thermal History of Sedimentary Basins* (eds. N. D. Naeser and T. H. McCulloh). Springer, New York, pp. 133–140.

Reitz A., Haeckel M., Wallmann K., Hensen C. and Heeschen K. (2007) Origin of salt-enriched pore fluids in the northern Gulf of Mexico. *Earth Planet. Sci. Lett.* **259**, 266–282.

Richter F. M. and DePaolo D. J. (1987) Numerical models for diagenesis and the Neogene Sr isotopic evolution of seawater from DSDP Site 590B. *Earth Planet. Sci. Lett.* **83**, 27–38.

Richter F. M. and Liang Y. (1993) The rate and consequences of Sr diagenesis in deep-sea carbonates. *Earth Planet. Sci. Lett.* **117**, 553–565.

Rovere M., Ranero C., Sartori R., Torelli L. and Zitellini N. (2004) Seismic images and magnetic signature of the Late Jurassic to Early Cretaceous Africa-Eurasia plate boundary off SW Iberia. *Geophys. J. Int.* **158**, 554–568.

Schettino A. and Turco E. (2009) Breakup of Pangaea and plate kinematics of the central Atlantic and Atlas regions. *Geophys. J. Int.* **178**, 1078–1097.

Scholz F., Hensen C., Reitz A., Romer R. L., Liebetrau V., Meixner A., Weise S. M. and Haeckel M. (2009) Isotopic evidence ($^{87}Sr/^{86}Sr$, $\delta^{7}Li$) for alteration of the oceanic crust at deep-rooted mud volcanoes in the Gulf of Cadiz, NE Atlantic Ocean. *Geochim. Cosmochim. Acta* **73**, 5444–5459.

Scholz F., Hensen C., De Lange G. J., Haeckel M., Liebetrau V., Meixner A., Reitz A. and Romer R. L. (2010a) Lithium isotope geochemistry of marine pore waters – insights from cold seep fluids. *Geochim. Cosmochim. Acta* **74**, 3459–3475.

Scholz F., Hensen C., Lu Z. and Fehn U. (2010b) Controls on the 129I/I ratio of deep-seated marine interstitial fluids: 'Old' organic versus fissiogenic 129-iodine. *Earth Planet. Sci. Lett.* **294**, 27–36.

Somoza L., Díaz-del-Río V., León R., Ivanov M., Fernández-Puga M. C., Gardner J. M., Hernández-Molina F. J., Pinheiro L. M., Rodero J., Lobato A., Maestro A., Vázquez J. T., Medialdea T. and Fernández-Salas L. M. (2003) Seabed morphology and hydrocarbon seepage in the Gulf of Cadiz mud volcano area: acoustic imagery, multibeam and ultra-high resolution seismic data. *Mar. Geol.* **195**, 153–176.

Stein C. A. and Stein S. (1993) A model for the global variation in the oceanic depth and heat flow with lithospheric age. *Nature*, 359.

Stein C. A., Stein S. and Pelayo A. (1995) Heat flow and hydrothermal circulation. In *Seafloor Hydrothermal Systems: Physical, Chemical, Biological, and Geological Interactions* (eds. S. E. Humphris, R. A. Zierenberg, L. S. Mullineaux and R. E. Thomson). American Geophysical Union, Washington DC, pp. 425–445.

Steuber T. and Veizer A. (2002) Phanerozoic record of plate tectonic control of seawater chemistry and carbonate sedimentation. *Geology* **30**, 1123–1126.

Stoll H. M., Schrag D. P. and Clemens S. C. (1999) Are seawater Sr/Ca variations preserved in Quaternary foraminifera? *Geochim. Cosmochim. Acta* **63**, 3535–3547.

Sumner R. H. and Westbrook G. K. (2001) Mud diapirism in front of the Barbados accretionary wedge: the influence of fracture zones and North America – South America plate motions. *Mar. Pet. Geol.* **18**, 591–613.

Terrinha P., Matias L., Vicente J., Duarte J., Luis J., Pinheiro L., Lourenco N., Diez S., Rosas F., Magalhaes V., Valadares V., Zitellini N., Roque C. and Victor L. M. (2009) Morphotectonics and strain partitioning at the Iberian-Africa plate boundary from multibeam and seismic reflection data. *Mar. Geol.* **267**, 156–174.

Tomaru H., Lu Z., Snyder G. T., Fehn U., Hiruta A. and Matsumoto R. (2007) Origin and age of pore waters in an actively venting gas hydrate field near Sado Island, Japan Sea: interpretation of halogen and ^{129}I distributions. *Chem. Geol.* **236**, 350–366.

Toyos M. H., Medialdea T., León R., Somoza L., González F. J. and Meléndez N. (2016) Evidence of episodic long-lived eruptions in the Yuma, Ginsburg, Jesús Baraza and Tasyo mud volcanoes, Gulf of Cádiz. *Geo-Mar. Lett.* **36**, 197–214.

Von Herzen R. (2004) Evidence for continuing hydrothermal circulation in old crust. In *Hydrogeology of the Oceanic Lithosphere* (eds. E. E. Davis and H. Elderfield). Cambridge University Press, Cambridge, pp. 414–447.

Wheat C. G., Elderfield H., Mottl M. J. and Monnin C. (2000) Chemical composition of basement fluids within an oceanic ridge flank: Implications for along-strike and across-strike hydrothermal circulation. *J. Geophys. Res. Solid Earth* **105**, 13437–13447.

Wortel M. and Spakman W. (2000) Subduction and slab detachment in the Mediterranean-Carpathian region. *Science* **290**, 1910–1917.

Xu W. and Germanovich L. N. (2006) Excess pore pressures resulting from methane hydrate dissociation in marine sediments: a theoretical approach. *J. Geophys. Res.* **111**. https://doi.org/10.1029/2004JB003600.

Zitellini N., Rovere M., Terrinha P., Chierici F., Matis L. and Team A. B. (2004) Neogene through Quaternary tectonic reactivation of SW Iberian passive margin. *Pure Appl. Geophys.* **161**, 565–587.

Zitellini N., Gràcia E., Matias L., Terrinha P., Abreu M. A., DeAlteriis G., Henriet J. P., Dañobeitia J. J., Masson D. G., Mulder T., Ramella R., Somoza L. and Diez S. (2009) The quest for the Africa-Eurasia plate boundary west of the Strait of Gibraltar. *Earth Planet. Sci. Lett.* **280**, 13–50.

Associate editor: Marc Norman